Department of Physics and Astronomy

University of Heidelberg

Diploma thesis

in Physics

submitted by

Christian Nordhorn

born in Neuss

2010

Dissociative recombination of deuterated formyl cations

This diploma thesis has been carried out by *Christian Nordhorn*
at the
Max-Planck-Institut für Kernphysik
under the supervision of
Herrn Prof. Dr. Andreas Wolf

Kurzfassung

Dissoziative Rekombination deuterierter Formyl-Kationen

Dissoziative Rekombination stellt in interstellaren Medien den Hauptzerstörungsmechanismus für molekulare Ionen dar. Astrophysikalische Modelle und radioastronomische Untersuchungen sind auf Informationen über diesen Prozess angewiesen. Unter Anwendung der Methode sich gegenseitig überlappender Strahlen wurde am Schwerionen-Speicherring TSR des Max Planck Instituts für Kernphysik in Heidelberg eine Studie zur Molekülfragmentation von deuterierten Formyl-Kationen durchgeführt. Ein energieempfindlicher Detektor kam hierbei zum Einsatz und ermöglichte Messungen zur energieabhängigen Entwicklung der Verzweigungsverhältnisse der einzelnen Fragmentationskanäle und zur inneren Anregung der molekularen Rekombinationsprodukte. Die Interpretation der Daten stützt sich auf eine unabhängig durchgeführte Studie, die Erkenntnisse über die innere Anregung der Ausgangsmoleküle und des relativen Anteils des Isomers im Ionenstrahl einbrachte. Die experimentellen Ergebnisse stimmen mit Berechnungen elektronischer resonanter Zustände des molekularen Systems, über die die dissoziative Rekombination aller Voraussicht nach erfolgt, überein.

Abstract

Dissociative recombination of deuterated formyl cations

In interstellar media dissociative recombination is considered the principal destruction mechanism for molecular ions. Information about this process is very important in astrophysical modeling and therefore essential for radioastronomical probes. A molecular fragmentation study on the dissociative recombination of deuterated formyl cations has been performed applying the merged-beam technique provided by the heavy-ion storage-ring TSR at the Max-Planck-Institute for Nuclear Physics in Heidelberg. Utilizing a recently developed energy-sensitive imaging detector advanced investigations of the energy dependent evolution of the branching ratios into the different accessible fragmentation channels and the inner excitation of the molecular recombination products have been enabled. The interpretation of the data resorts to an independently performed relaxation study which yielded the inner excitation of the initial molecular ions and the abundance ratio of the isomer. The experimental results indicate correspondence to calculations on the molecular system, which determined electronic resonant states through which the dissociative recombination is considered to proceed.

Contents

1. Introduction

The recombination of a positive molecular ion with an electron leading to the dissociation of the compound system is the most complex of gas-phase reactions resulting in the production of neutral molecules. It is called dissociative recombination and applicable to a wide range of physical areas comprising chemical physics, atmospheric physics and molecular astrophysics [1]. Due to its particular importance to the chemistry of interstellar space this process plays a key role in modeling astrophysically relevant plasmas. Thus the analysis of radioastronomical probes requires extensive comprehension of fundamental process characteristics, which are subject to both experimental and theoretical investigations.

The main focus of these investigations is on the determination of the energy positions and the structures of electronic resonant states, whose existence is considered the essential precondition for the occurrence of dissociative recombination. An electron collision, which does not lead to an interim transition of the system into one of these resonant states, cannot mediate between the electron and the intramolecular motions, whose typical time scales are not compatible. The coupling between the two reactants is insufficiently strong for an efficient energy transfer. However this required energy transfer becomes efficient for resonant electron collisions, in which resonant states are occupied. In this case the electron is captured by and temporarily attached to the molecular ion. The conversion of the electron's kinetic energy into potential energy of the neutral compound system and the subsequent conversion into kinetic energy of the recombination products proceed efficiently. Therefore the study of the dissociative recombination of a given system is the study of the resonant states of this system [2].

The molecular system observed in the present experiment is the deuterated formyl cation DCO^+. It presents itself as a particularly suitable test object because of its abundance in interstellar media and its strong integration into the fundamental chemical processes. The electronic resonant states of formyl cations have been determined in a recent theoretical investigation [3].

The experimental investigation of the dissociative recombination of deuterated formyl

cations is the main subject of the present thesis. A storage-ring experiment has been performed applying the merged beam technique provided by the Test Storage Ring TSR at the Max-Planck-Institute for Nuclear Physics in Heidelberg. The neutral recombination products are observed on an event-by-event basis with the help of a recently developed energy-sensitive surface-barrier detector which introduces mass identification of individual recombination products and a simultaneous determination of the fragment positions in the detector plane by coincidence imaging. This enables advanced investigations of the final state branching ratios into the different fragmentation channels, the inner excitation of the neutral molecular fragments and the dissociation kinematics.
The thesis intends to discuss the experimental and to outline the theoretical approach of specifying the fundamental features of the molecular process dissociative recombination. It aims to check the consistence of both approaches by comparing the results obtained for an investigation of deuterated formyl cations.
The physical properties of the formyl cations and the specific features of their dissociative recombination are presented in the following chapter. It deals with the basic principles of the molecular process and compiles the relevant information about the test object.
Chapter three focuses on the theoretical approach of studying dissociative recombination. The essential ideas of the theoretical calculations are followed resorting to the most recent study on formyl cations [3]. The theoretically obtained results are summarized and interpreted in detail.
The experimental approach is subject to chapters four and five. An independently performed relaxation study of the deuterated formyl cations, which has a preliminary function concerning the molecular fragmentation study, is presented. With special regard to the developed detector system the experimental technique of the present investigation is discussed. Chapter four closes by pointing out the critical aspects of the analysis of the experimentally obtained results. These results are introduced in chapter five and compared to results obtained in other experiments. The comparison to the theoretical results is the concluding aspect of this chapter.
A summary of the two approaches and their comparison is given in the final chapter.

2. Dissociative recombination of deuterated formyl cations

In interstellar media dissociative recombination is considered the principal destruction mechanism for molecular ions. Thus astrophysical models impart basic process characteristics and consequently rely on experimental and theoretical findings on the properties of this process regarding the relevant molecules. Among these molecules are deuterated formyl cations DCO^+, which are one of the primary molecular ions involved in the essential processes of molecular cloud chemistry.
The relevant chemical processes leading to the formation of DCO^+ in astrophysically relevant plasmas are presented in the first section, which deals with the properties of the molecular ion in general. The focus of the second section is on the process features starting at general considerations and advancing to concrete information about the dissociative recombination of deuterated formyl cations.

2.1 Deuterated formyl cations

The formyl cation HCO^+ is among the most abundant and important molecular ions in interstellar media. It is highly involved in the chemical processes and considered to be second only to H_3^+ in importance as far as interstellar molecular ions are concerned [1]. Its spectrum was first observed in 1970 by means of radioastronomy [4] and identified [5] as the $J = 1$ - 0 rotational transition. In astrophysically relevant plasmas the main production and depletion processes of HCO^+ can be traced back to the basic first steps of molecular cloud chemistry [1], which proceed from slow cosmic ray ionization of hydrogen molecules H_2. In a second step H_3^+ molecular ions are generated in a rapid ion-molecule reaction. H_3^+ acts as a proton donator to the majority of atoms and molecules abundant in molecular clouds due to its low proton affinity. A proton exchange with carbon monoxide finally leads to the formation of formyl cations. The corresponding reactions are listed.

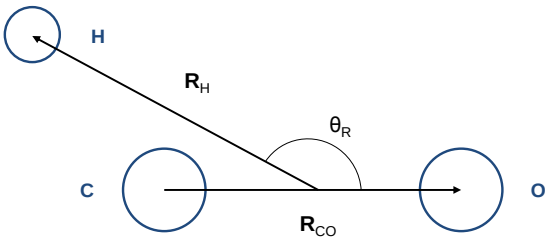

Figure 2.1: *Definition of the Jacobi coordinates for formyl cations.* $\boldsymbol{R}_{CO}$ *denotes the distance between the carbon and the oxygen nucleus. The distance between the hydrogen and the center of* $\boldsymbol{R}_{CO}$ *is given by* $\boldsymbol{R}_H$*. The Jacobi angle* θ_R *determines the position of the proton relative the C-O bond and therefore the configuration of the molecular system.*

$$\begin{aligned} H_2 + \gamma &\longrightarrow H_2^+ + e^- + \gamma' \\ H_2 + H_2^+ &\longrightarrow H_3^+ + H \\ H_3^+ + CO &\longrightarrow HCO^+ + H_2 \end{aligned}$$

The formyl cations are characterized by linear equilibrium geometry. One of the possible mathematical descriptions of the molecular system is displayed in figure 2.1.
The Jacobi coordinates comprise two vectors and one angle. The first vector $\mathbf{R}_{CO}$ represents the distance between the carbon and the oxygen atom, whose common triple bond has a strong dipole moment. Starting at the center position of this first vector, the second vector $\mathbf{R}_H$ points at the hydrogen atom. The Jacobi angle θ_R defines the relative direction of both vectors.
Regarding these definitions the molecular ion is in the HCO^+ configuration and called formyl cation if θ_R amounts to 180° and the hydrogen atom is attached to the carbon atom. The isoformyl configuration HOC^+ corresponds to $\theta_R = 0°$. In this case the hydrogen and the oxygen atom have a common bond.
There are differing arrangements [6, 7], which θ_R-value marks the transition from one configuration into the other. As far as any of these arrangements is used exclusively and consistently within a study on the molecular system, this variety of different definitions will not cause any reason for unclearnesses. Obviously the same holds for varying definitions of the coordinate system as will be outlined in 3.1.
The process in which the configuration of the cation changes is called isomerization. It is initiated by collision processes or proceeds from highly excited molecular ions. The isoformyl cation HOC^+ thus is generated in collision processes, from which one is shown exemplarily. A second source for its generation is the reaction of H_3^+ and carbon monoxide

already referred to for the production of formyl cations.

$$\begin{aligned} HCO^+ + H_2 &\longrightarrow HOC^+ + H_2 \\ H_3^+ + CO &\longrightarrow HOC^+ + H_2 \end{aligned}$$

The interstellar abundance ratio of the two isomers has been found in several experiments to be $70 \leq \frac{[HCO^+]}{[HOC^+]} \leq 360$ [8].
Because of technical reasons the experimental study is performed using deuterated formyl cations DCO^+. This will be discussed in chapter 4.
The production of deuterated formyl cations DCO^+ and isoformyl cations DOC^+ proceeds similarly replacing the proton donator H_3^+ by the deuterium comprising molecular ion H_2D^+.

$$\begin{aligned} H_2D^+ + CO &\longrightarrow DCO^+ + H_2 \\ H_2D^+ + CO &\longrightarrow DOC^+ + H_2 \end{aligned}$$

In correspondence to the considerations concerning HCO^+ a configuration change by isomerization result from a collision process or from a sufficiently high excitation of the system.
The potential energy surface of the isomeric system is displayed as a function of the Jacobi angle in figure 2.2. It shows a slice through a calculated, originally multidimensional surface, which additionally considers the dependence on the two vectors defined in figure 2.1. The potential energy surface has been determined theoretically in [6].
The two minima at 0° and 180° denote the linear equilibrium geometries existing for the two possible configurations DCO^+ and DOC^+, respectively. In the case of the metastable isoformyl configuration the repelling forces created by the potential become relevant only for angle deviations from the linear geometry exceeding 20°. However the configuration of the cation in the formyl configuration is defined clearly.
The metastable ground state is situated 1.7 eV above the energetically favored ground state of the isomeric system. The barrier to isomerization is represented by the maximum and amounts to 3.3 eV. It is located at an angle of approximately 96°.
The theoretical calculations carried out for the DCO^+/DOC^+ system [6] additionally derived the tunneling probabilities through the barrier to isomerization. Only the vibrational levels which lie less than 120 meV below the energy of the saddle point have finite wave function amplitudes on both sides of the potential barrier and are therefore expected to have a finite tunneling probability [7]. Consequently the excitation of the DOC^+ molecule must exceed 3.18 eV for isomerization to proceed independently of a collision process.

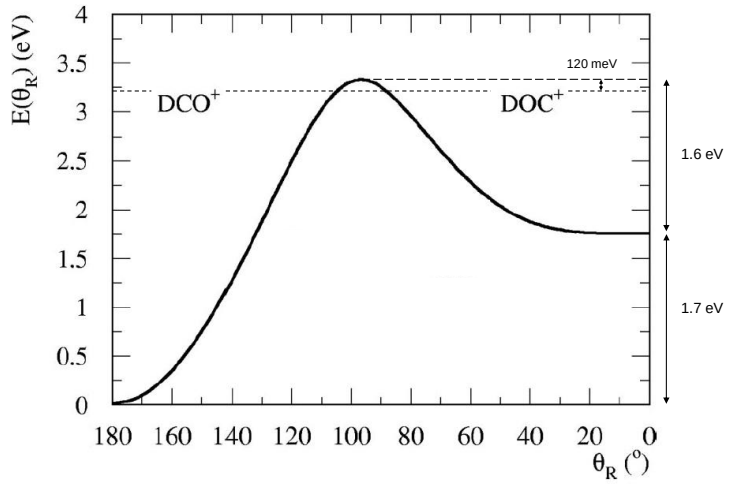

Figure 2.2: *Slice through the multidimensional potential energy surface of the isomeric system. The deuterated isoformyl cation is situated 1.7 eV higher in energy with a barrier to isomerization of 1.6 eV. A finite tunneling probability have been found only for energy levels which are situated less than 120 meV below the barrier to isomerization.*

2.2 Dissociative recombination of molecular ions with electrons

Dissociative recombination of molecular ions with electrons is also referred to as electron capture to dissociation. It is a primarily chemical process, which is initiated by an electron capture and proceeds through an intermediate formation of an unstable neutral state. The process is particularly efficient for resonant electron-ion collisions. In the scheme outlined in the previous section 2.1 dissociative recombination is regarded as a process for molecule formation representing the final step of the production mechanism.
This section deals with the fundamental process characteristics of dissociative recombination. They will be presented in general and specified for deuterated formyl cations.

2.2.1 Fundamental process characteristics

Dissociative recombination is initiated by the capture of a free electron. The electron is transferred to a bound state of the molecular system, if the excess energy of the recombination process can be compensated. An enduring neutralization of the positive molecular ion requires a stabilization process, which proceeds after the formation of the unstable neutral state.

The stabilization can be achieved by a re-establishment of the initial state of the molecular ion. The system is deexcited by autoionization and the product channel comprises a free electron, which has temporarily been bound to the system, and the molecule. The typical order of magnitude for the lifetime of an excited resonant state against autoionization will be given in 3.1. This process obviously is not considered as dissociative recombination.
The competing stabilization process is far more efficient, since it makes use of the internal molecular structure. The excess energy transferred by the electron capture is compensated by breaking one or several bonds between the constituents of the molecule. For this electron-collision initiated dissociation process two different mechanism have been proposed.

1. **Direct mechanism** (Bates, 1950) [9]

   The direct mechanism consists of two steps. In the first step the electron is captured by the molecular ion resulting in the formation of an unstable neutral molecule. The electron does not interact with the disproportinately heavier nuclei but with the electron cloud. Subsequently this molecule rapidly dissociates in the second step. The fast dissociation process decisively reduces the probability for an autoionization process, in which the electron is transferred back to the continuum.

   According to the present status of the analytical discussion a resonant state, which crosses the ion ground potential close to its minimum, is considered as a precondition for this direct mechanism.

2. **Indirect mechanism** (Chen and Mittleman, 1967) [10]

   A series of Rydberg states converging to the ion core plays an essential role in the indirect mechanism of dissociative recombination. The electron is captured into one of these Rydberg states. This results in an excitation of a vibrational mode. The Rydberg state then is predissociated by an electronically doubly-excited, repulsive state.

Since there are two indistinguishable processes leading to the same product, interference is expected resulting in structures in the absolute cross section as a function of energy and similar oscillations in the final state distributions [1].
Both proposals avoid the problem of the weak coupling between the electronic and the nuclear motions and outline a process, in which the energy transfer during the dissociative recombination can proceed efficiently. This especially holds for resonant electron-ion collision in which the probability for a certain transition is resonantly increased because

of corresponding energies. The energy conservation at zero relative electron-ion collision energy can be formulated as

$$E_{kin} = E_{KER} + E_{vib,DCO^+} + E_{rot,DCO^+} - E_{e,CO} - E_{vib,CO} - E_{rot,CO}$$

exemplarily for the case of the reaction $DCO^+ + e^- \longrightarrow D + CO$.
E_{kin} denotes the kinetic energy available to the recombination products. It depends on the energy E_{KER} released in the dissociation process and the rovibrational excitation of the initial molecular ion, which is taken into account by E_{vib,DCO^+} and E_{rot,DCO^+}. The three terms, which reduce the kinetic energy E_{kin} define the electronical, vibrational and rotational excitation of the molecular fragment.
Since there are characteristic discrete values for the energy release E_{KER} the kinetic energy E_{kin} also represents a discrete quantity depending only on quantized variables apart from E_{KER}.
In case of elevated collision energies the increased energy transfer to the molecular system is considered by an additional variable. This additional variable besides transforms E_{kin} into a continuous quantity.

2.2.2 Specific process features regarding deuterated formyl cations

For a given molecular system the properties of the dissociative recombination can be specified concerning the accessible fragmentation channels and the characteristic energy releases E_{KER}.
Regarding deuterated formyl cations DCO^+ the only exoergic fragmentation channel comprises three possibilities for the electronic excitation of the molecular recombination product carbon monoxide.

$$\begin{aligned} DCO^+ + e^- &\longrightarrow CO(X\ ^1\Sigma^+) + D(^2S) + 7.25\ eV \\ &\longrightarrow CO(a\ ^3\Pi_r) + D(^2S) + 1.24\ eV \\ &\longrightarrow CO(a'\ ^3\Sigma^+) + D(^2S) + 0.38\ eV \end{aligned}$$

It consequently shows three characteristic values for the energy release. The $X\ ^1\Sigma^+$ state is the electronic ground state of carbon monoxide. According to the energy balance derived in 2.2.1 the given energy values can be reduced due to rovibrational excitation. The values for DCO^+ have been adopted from data on HCO^+ [11] having performed a

slight modification, because the zero point energies of the initial molecular ions are shifted due to the different reduced masses.
The second two-body channel and the three-body channel are endoergic.

$$\begin{aligned} DCO^+ + e^- &\longrightarrow DC + O \text{ - } 0.17 \text{ eV} \\ &\longrightarrow D + C + O \text{ - } 3.90 \text{ eV} \end{aligned}$$

The energy value given for the fragmentation into the three atomic constituents denotes the threshold corresponding to the minimum energy required for a break of both bonds. This minimum is reached if the dissociation proceeds from a break of the D-C bond leading to the maximum energy release. The triple bond between the carbon and the oxygen atom consequently has a binding energy of 11.15 eV.
The dissociative recombination $DCO^+ + e^- \longrightarrow DO + C$ is very unlikely because the deuterium is bound to the carbon in the case of the deuterated formyl cations. A fragmentation leading to DO as recombination product cannot proceed unless there is a simultaneous isomerization. However regarding deuterated isoformyl cations the considered channel exists.

$$DOC^+ + e^- \longrightarrow DO + C + 0.72 \text{ eV}$$

It is exoergic and can completely be assigned to the dissociative recombination of DOC^+ following the outlined considerations.
Theoretical calculations and an independent experimental study, dealt with in sections 3.2.1 and 4.1 respectively, confirm the linear molecule structure of both isomers and also exclude the possibility of an isomerization during the dissociation process.
In correspondence the fragmentation into DC and O can be assigned to the dissociative recombination of DCO^+.
The exoergic two-body channel and the three-body channel are open for both isomers. Thus the following reactions complete the list of accessible fragmentation channels.
Figure 2.3 summarizes the energy information about the dissociation channels and exemplarily displays the positions of the lowest electronic resonant states for different symmetries of the system, which have been determined theoretically for HCO^+ as discussed in section 3.1.
The two configurations of the isomeric system are separated by the barrier to isomerization. All dashed lines refer to the (D+CO)-fragmentation channel and denote different inner excitations of carbon monoxide. The gaps between the dashed lines are filled by

$$
\begin{aligned}
\mathrm{DOC^+ + e^-} &\longrightarrow \mathrm{CO(X\ ^1\Sigma^+)} + \mathrm{D(^2S)} + 8.99\ \mathrm{eV} \\
&\longrightarrow \mathrm{CO(a\ ^3\Pi_r)} + \mathrm{D(^2S)} + 2.98\ \mathrm{eV} \\
&\longrightarrow \mathrm{CO(a'\ ^3\Sigma^+)} + \mathrm{D(^2S)} + 2.12\ \mathrm{eV} \\
&\longrightarrow \mathrm{CO(d\ ^3\Delta_i)} + \mathrm{D(^2S)} + 1.47\ \mathrm{eV} \\
&\longrightarrow \mathrm{CO(e\ ^3\Sigma^-)} + \mathrm{D(^2S)} + 1.23\ \mathrm{eV} \\
&\longrightarrow \mathrm{CO(A\ ^1\Pi)} + \mathrm{D(^2S)} + 0.96\ \mathrm{eV}
\end{aligned}
$$

$$
\mathrm{DOC^+ + e^-} \longrightarrow \mathrm{D + C + O} - 2.18\ \mathrm{eV}
$$

densely lying vibrational states of carbon monoxide. The energy positions of these vibrational states are listed in [12].

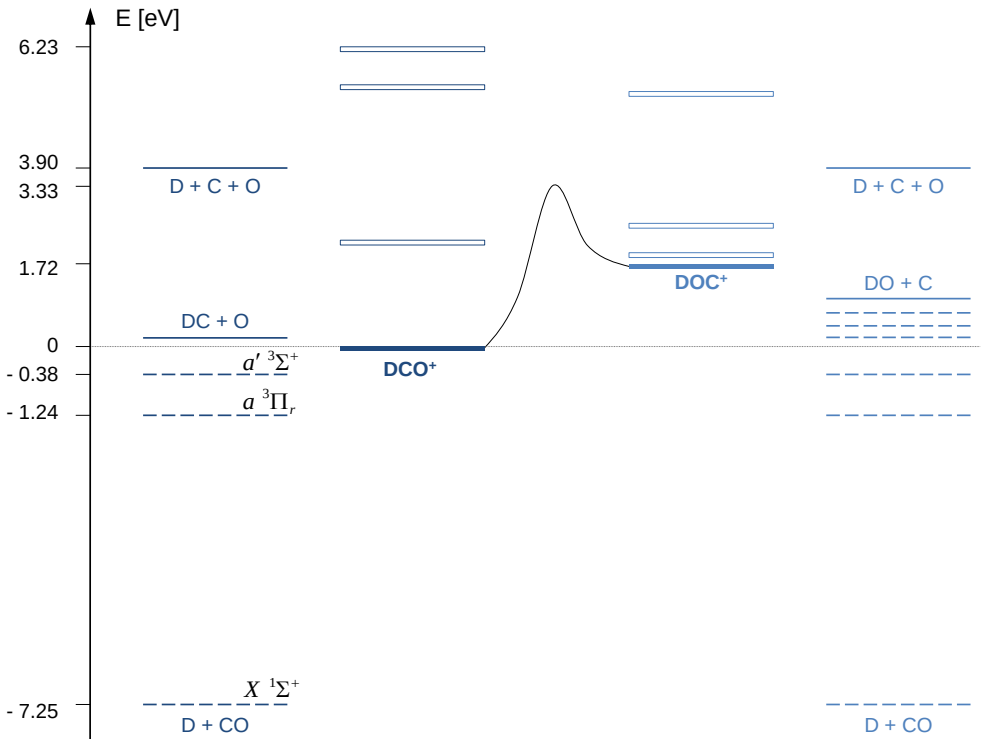

Figure 2.3: *Summary of the energy level positions of the isomeric system. The subsystems, which are divided by the barrier to isomerization, are colored differently. The dashed lines represent the different electronically excited states of carbon monoxide. Vibrational states of carbon monoxide occupie the gaps between these electronical levels. The lowest electronic resonant states of different symmetries are displayed for both systems above the respective ground states.*

Moreover the experimental and theoretical studies of the HCO^+ ion convey an idea of two further aspects of the dissociative recombination of DCO^+.
Several measurements agree on a relatively large absolute rate of around 2×10^{-7} cm^3s^{-1} at 300 K. However the temperature dependence of the measured rates varies in the different experiments, comprising stationary afterglows [13], flowing afterglows [14] and a merged-beam study [15].
Theoretical calculations [16] revealed no indications for a diabatic state crossing the ion ground state. Thus the indirect mechanism seems to be favored in case of formyl cations and the initial capture of the electron most likely take place to a Rydberg state.

3. Theoretical approach

The theoretical approach of studying dissociative recombination focuses on the calculation of the electronic resonant states. Their energy positions and the shape of their potential energy surfaces enable to draw conclusions concerning the accessibility of certain fragmentation channels and probabilities that dissociative recombination might proceed through the calculated states.
The diagrams presented in this chapter are slices from multidimensional potential energy surfaces which resulted from calculations carried out on HCO^+ for different symmetries of the system [3]. As will be outlined in chapter 4 the experimental investigation requires the use of deuterated formyl cations because of technical reasons. Since the electronic forces of both systems are identical the qualitative significance of the calculation results is maintained for an application on the measurement data. Nevertheless it is advisable to keep in mind, that the interpretation is slightly different due to the varied reduced mass of the wavepackets, which play a role in the analysis of the potential energy surfaces as explained in section 3.2.
The calculation of the electronic resonant states is the main subject of this chapter. Moreover the interpretation of the calculated potential energy surfaces and an immediate application of the data as a basis for a simulation of the energy-dependent branching-ratio evolution will be discussed.

3.1 Calculation of the electronic resonant states

The determination of the electronic resonant states of the recombined neutral system is the central aspect of the theoretical approach studying dissociative recombination.
It is based on two consecutive calculations. In a first step structure calculations of the system are carried out, from which the following three types of states are obtained.

1. Rydberg states converging to the ion ground state (adiabatic states)
2. states trying to describe the ionization continuum

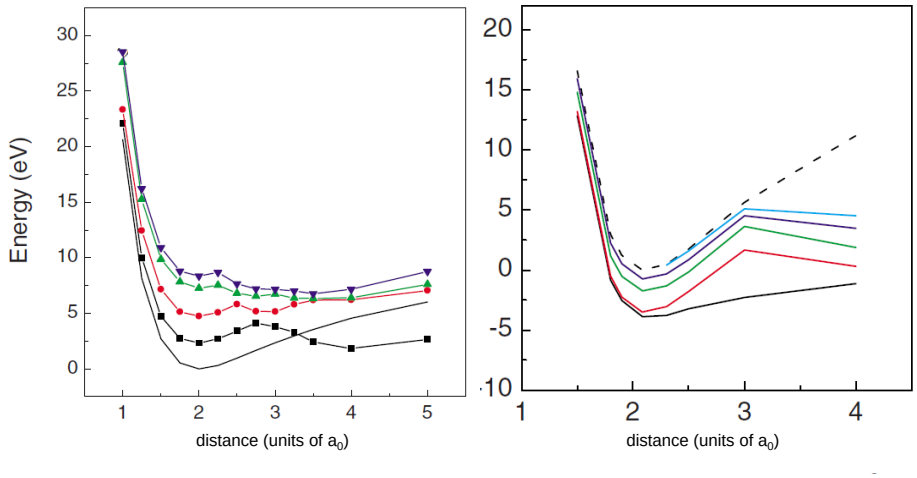

Figure 3.1: *Neutral resonant states (left plot) and adiabatic states (right plot) obtained from structure calculations. The solid black line and the dashed black line, respectively, represent the ion ground-state potential. [3]*

3. Rydberg states converging to excited states of the ion (resonant states)

Figure 3.1 conveys the general idea of adiabatic states and resonant states. Both belong to a Rydberg series converging to different states of the ion system.
The electronic resonant states are not bound states of the system and have a finite lifetime. To extract their energy position electron-scattering calculations are carried out in a consecutive second step based on the derived structure information. For these calculations a slightly modified coordinate system is used than for the calculations of the energy potential surface of the isomeric system presented in section 2.1. The three internal coordinates of the system are the two bond lengths between the carbon nucleus on one side and the proton and oxygen nucleus, respectively, on the other side and the angle between the two vectors. The modified coordinate system is displayed in figure 3.2.
As will be discussed in more detail in section 3.2.1 an examination of the bending angle in the Franck-Condon region of the system proved that only the two bond lengths are relevant variables for interpretations of the calculation results. Consequently the bending angle as the third variable can be excluded and the calculations can be carried out at linear geometry. Figure 3.3 displays the configuration of the molecule relevant for the calculations and declares the equilibrium bond lengths. It is possible to extract the dependence of the potential energy surfaces already from structure calculations carried out for different molecule geometries.
Besides the autoionization widths of the calculated electronic states have been determined within the theoretical analysis. Their determination serves as a cross-check and aims

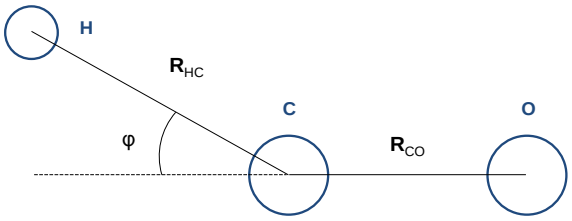

Figure 3.2: *Coordinate system employed to carry out electron-scattering calculations on HCO^+. The definition of the distance $\boldsymbol{R}_{CO}$ also is found in the Jacobi coordinate system. $\boldsymbol{R}_{HC}$ denotes the distance between the hydrogen and the carbon nucleus. The angle ϕ determines the configuration of the system.*

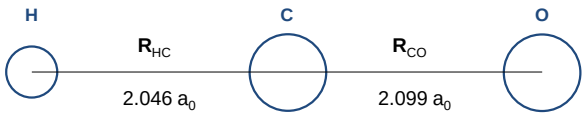

Figure 3.3: *Equilibrium bond lengths of the system in the linear configuration. The bending angle does not represent a relevant variable of the system for the calculations of interest.*

to confirm that autoionization is not a relevant stabilization process competing with dissociative recombination.

The largest values for the resonant states of different symmetries are given in table 3.1 to derive a lower estimation for the lifetime of the respective states against autoionization.

The estimation of the lifetime τ of the resonant states against autoionization is based on the formula $\tau = \frac{\hbar}{\Gamma}$, in which Γ denotes the autoionization width. This leads to a lower limit of $\tau \approx 2.6$ fs for the largest value of $\Gamma = 0.25$ eV.

Symmetry	Autoionization width (eV)
$^2\Sigma^+$	0.027
$^2\Pi$	0.25
$^2\Delta$	0.085

Table 3.1: *Autoionization widths of the resonant states of HCO. For each symmetry considered in the theoretical study the largest value is given. [3]*

3.2 Interpretation of the calculated energy potential surfaces

The plots presented in this section result from the combination of structure and electron-scattering calculations, as outlined in the previous section. They display slices of originally obtained multidimensional potential energy surfaces as a function of one of the bond lengths keeping the second variable of the system fixed at its equilibrium value. Two diagrams complement each other and convey a general idea of the two-dimensional surface assuming that there are only slight deviations of the potential for a simultaneous change of both bond lengths.

The interpretation of two complementary diagrams makes use of the striking significance of the physical concept of potentials. A single wavepacket is assumed to be originally located on the ground-state potential at the equilibrium distance in both diagrams, which corresponds to the minimum of each curve. As the result of a resonant electron collision this wavepacket is vertically transferred into the electronic resonant state with the corresponding energy. In this situation the determining factors for the movement of the wavepacket on the potential energy surface are the potential shape in the Franck-Condon region located around the equilibrium distance and the gradient at the equilibrium distance. The steeper the gradient is, the stronger is the repulsive force the wavepacket experiences after the excitation. The shape of the potential additionally decides whether the repulsive force is sufficient to lead to an increase in one of the variable coordinates, each of them represented by one of the two diagrams. The increase of a variable is equivalent to the dissociation of the corresponding molecular bond.

Figure 3.4 gives an example for the graphical presentation of the calculation results. In the left plot the C-O coordinate is kept fixed at its equilibrium value. The graphs display the energy potential evolution as a function of the H-C coordinate. In the right plot the same potential surfaces are plotted as a function of the C-O coordinate.

Following this train of thought the two diagrams help to understand the dissociation mechanism of the recombined neutral molecule qualitatively. In this model the different accessible fragmentation channels can be distinguished by determining which bond length preferably will increase to a decisive extent, indicating a dissociation of this bond, and how fast this dissociation process will proceed. Regarding a linear molecule with two variable bond lengths a dissociation along one of the coordinates will lead to a two-body breakup of the system. If both coordinates show a comparable potential surface evolution, a three-body breakup of the system can be expected. In this case both bonds break.

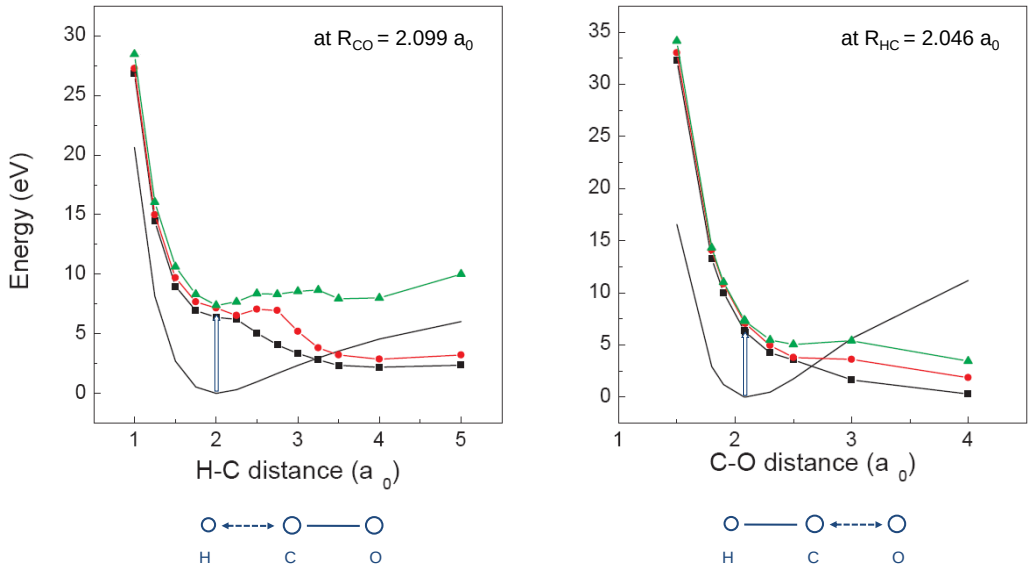

Figure 3.4: *Two complementary diagrams convey an idea of the multidimensional energy potential surface. The vertical transition to the black curve is displayed examplarily. The fixed distances are kept at their equilibrium values. [3]*

Calculations on the quantum dynamics of the system have not yet been performed. There are no data about the efficiency of this process. An interpretation of the results obtained so far on the theoretical sector consequently is restricted to this equivocal argumentation. Nevertheless, the energy positions of the resonant states are determined. Moreover it is possible to figure out which fragmentation channel will occur if the system is resonantly excited to one of these electronic states.

3.2.1 Resonant states as a function of the bending angle

The structure calculations already allow to determine the shape of the resonant state potentials as a function of the bending angle ranging from 0° to 20°.

The potential energy surfaces as a function of the bending angle in the Franck-Condon region of the system are relatively flat which indicates that a wavepacket placed on one of the calculated surfaces probably does not proceed any movement which may lead to a different configuration of the system. Consequently the number of internal coordinates can be reduced leaving only the two bond lengths in a linear geometry as parameters of the system.

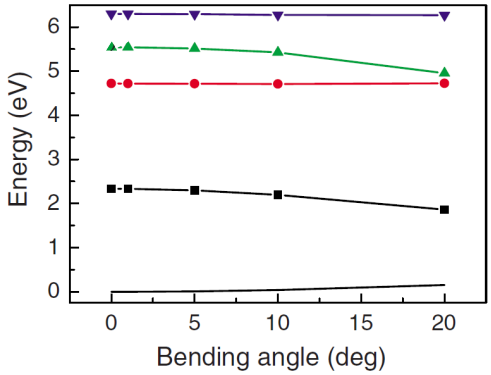

Figure 3.5: *Potential energy surfaces of different symmetries as a function of the bending angle for constant radial coordinates. The solid black line represents the ion ground potential. [3]*

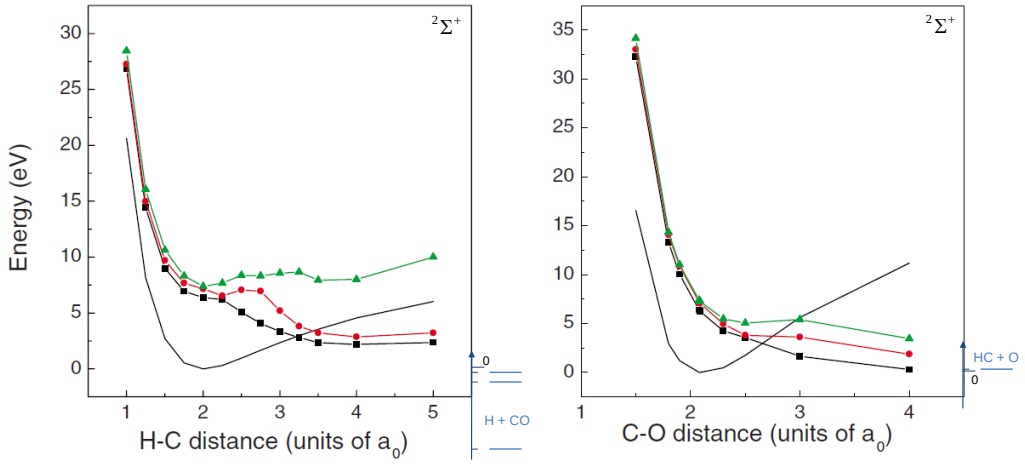

Figure 3.6: *Resonant states of HCO of $^2\Sigma^+$ symmetry. The graphs clearly show avoided crossings between attractive and repulsive resonant states. The energetically lowest state lies 6.23 eV above the ion ground potential (solid black line). In addition the energy positions of the possible final levels are plotted for both diagrams. [3]*

3.2.2 Electronic resonant states of HCO

The three energetically lowest resonant states of $^2\Sigma^+$ symmetry have been calculated at linear geometry and are displayed in figure 3.6.

In the first diagram the potential energy surfaces of the electronic resonant states are shown as a function of the H-C distance and for fixed C-O distance at its equilibrium value. The second diagram complements the presentation of the results by showing the potential energy surfaces as a function of the C-O coordinate. In this case the H-C bond

length remains constant at its equilibrium value. Identically colored curves correspond to each other. The black line represents the ion ground potential. The energy positions of the final levels, which can be reached by following the resonant states, are shown additionally. For the dissociation into H and CO there are three different electronical excitations of the molecular recombination product carbon monoxide possible as discussed in section 2.2.2. The essential aspects, which become recognizable in the graphical presentation, can be summarized as follows.

1. No resonant state crosses the ion ground potential close to its minimum.
2. There are crossings between dissociative resonant states and the ion ground potential at larger internuclear distances.
3. As a function of the C-O coordinate all calculated resonant states are repulsive.

Following the train of thought outlined at the beginning of the section the data presented in the first plot, which shows the resonant states as a function of variable H-C coordinate, can be interpreted in the following way. Assuming a wavepacket which originally is located at the ion ground state and then lifted to one of the resonant states, it probably will not perform any movement decisive for dissociation of the system, which is equivalent to an increase of one of the coordinates. There is a local minimum in the potential energy surface and no steep gradient exists. However for variable C-O coordinate all three resonant states are repulsive with relatively steep gradients at the equilibrium distance indicating a dissociative character. A wavepacket, which is virtually placed on one of these surfaces, immediately will begin to move to larger internuclear distances once the electron is attached to the system. Consequently the diagrams suggest a dissociation of the system following the C-O dissociation pathway for all calculated resonant states.
In accordance to the presentation of the calculation results for $^2\Sigma^+$ symmetry the four energetically lowest resonant states of $^2\Pi$ symmetry are displayed in the two plots of figure 3.7.
The characteristic features of the four curves correspond to the aspects stated for the previous plots. The resonant states do not cross the ion ground state close to its minimum but at larger internuclear distances. All resonant states are repulsive as a function of the bond length between the carbon and the oxygen nucleus. Again there are clear indications for a breakup of the C-O bond as consequence of an increase of the corresponding internuclear distance. The gradients of the potential energy surfaces at the equilibrium distance of the ion are considerably steeper in the second plot. However the curves for variable H-C distance do not cause any movement of a wavepacket.

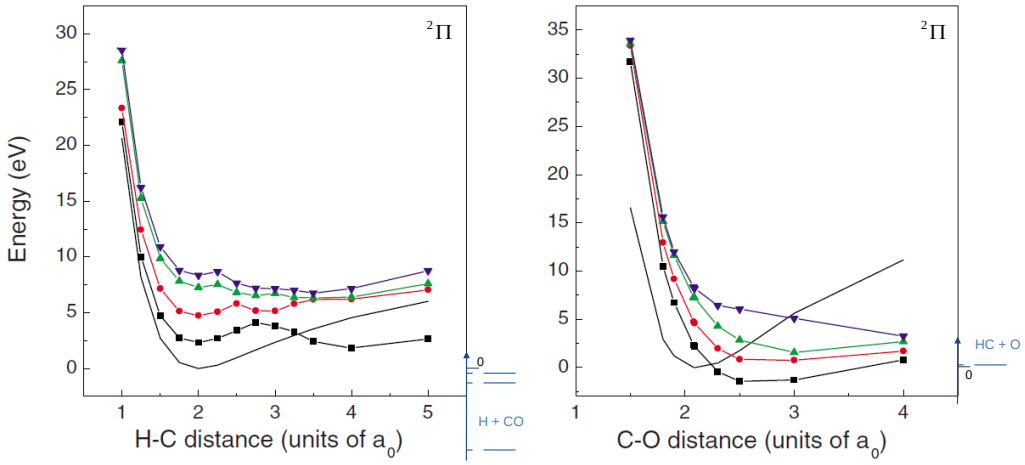

Figure 3.7: *Resonant states of HCO of* $^2\Pi$ *symmetry. The solid black line represents the ion ground potential. Again avoided crossings are found. At equilibrium geometry of the ion the energy of the lowest state amounts to 2.21 eV. For both diagrams the energy positions of the possible final levels are displayed. [3]*

The calculation results additionally comprise data for resonant states of $^2\Delta$ symmetry. The corresponding plots do not contain further features. They will be referred to in section 5.3 for a comparison between the experimental and the theoretical results.

3.2.3 Electronic resonant states of HOC

The resonant states of HOC have also been determined for $^2\Sigma^+$, $^2\Pi$ and $^2\Delta$ symmetry. Exemplarily the results for the $^2\Sigma^+$ symmetry are presented in figure 3.8 in order to figure out in which way they differ from the results obtained for HCO. Again the calculations have been carried out for linear geometry. The arguments for focusing on the two bond lengths as relevant variables of the system, which are given in section 3.2.1 also hold for the isomeric system.

The three states lowest in energy are displayed. A comparison of this plot with the plots for HCO leads to the following central aspects. In accordance to the previous results all resonant states as a function of the radial coordinate, which do not state the distance to the hydrogen nucleus, are repulsive. In the present case the plots indicate dissociation pathways along the O-C coordinate. In contrast to the previous results the energy positions of the states are much lower. This also applies for the resonant states of different symmetries, which are not presented in this comparison. Considering the energy values at the equilibrium distance of the ion the lowest state for HCO has a $^2\Pi$ symmetry and is 2.21 eV above the ion. For HOC the lowest resonant state is a $^2\Delta$ state, which is

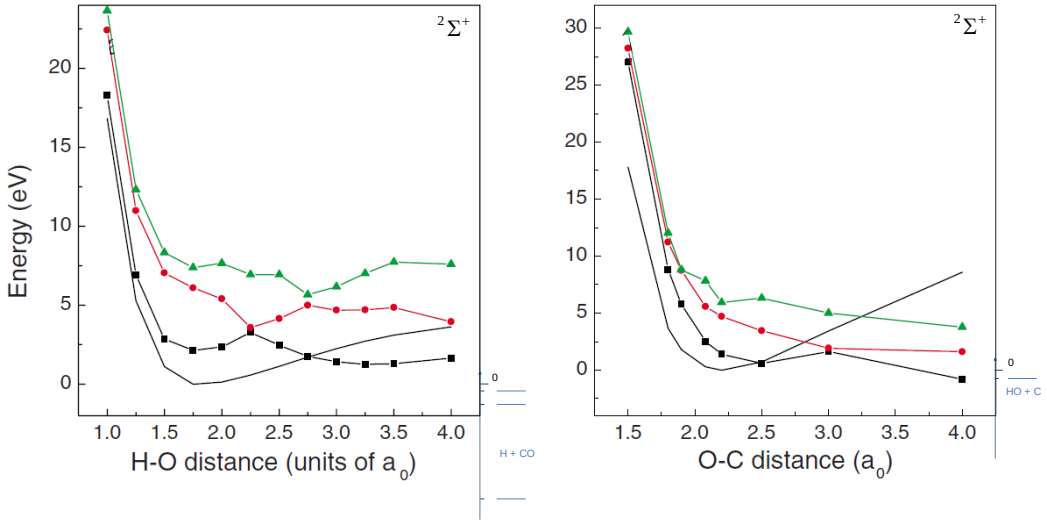

Figure 3.8: *Resonant states of HOC of $^2\Sigma^+$ symmetry. The ion ground potential is denoted by the solid black line. Identically colored curves represent the same state. At equilibrium geometry of the ion the energy of the lowest state amounts to 0.84 eV. The energy positions of the final levels indicate that both dissociation pathways lead to exoergic reactions. [3]*

0.23 eV above the ion at the equilibrium structure. Moreover there are several resonant states, which cross the ion in the Franck-Condon region. Only one of these states is of $^2\Sigma^+$ symmetry and displayed in the plot.

3.3 Simulation of the energy-dependent branching ratio evolution

Based on the calculated resonant states the collision-energy dependent evolution of the branching ratios has been simulated assuming a constant ratio of $\frac{[HCO^+]}{[HOC^+]} = 9$ between the two isomers. This latter assumption has been experimentally proven as will be shown in section 4.1.

The simulation has been carried out by Åsa Larson. It resorts to the determination of the multidimensional potential energy surfaces presented in [3] and includes all three calculated symmetries $^2\Sigma^+$, $^2\Pi$ and $^2\Delta$. The dynamics of wavepackets placed on the resonant potential energy surfaces are followed and analyzed with regard to the resulting dissociation pathways. Within the simulation the resonant electronic states are considered to be a necessary precondition for dissociative recombination to occur.

Figure 3.9 displays the simulated evolution of the branching ratios into the four fragmen-

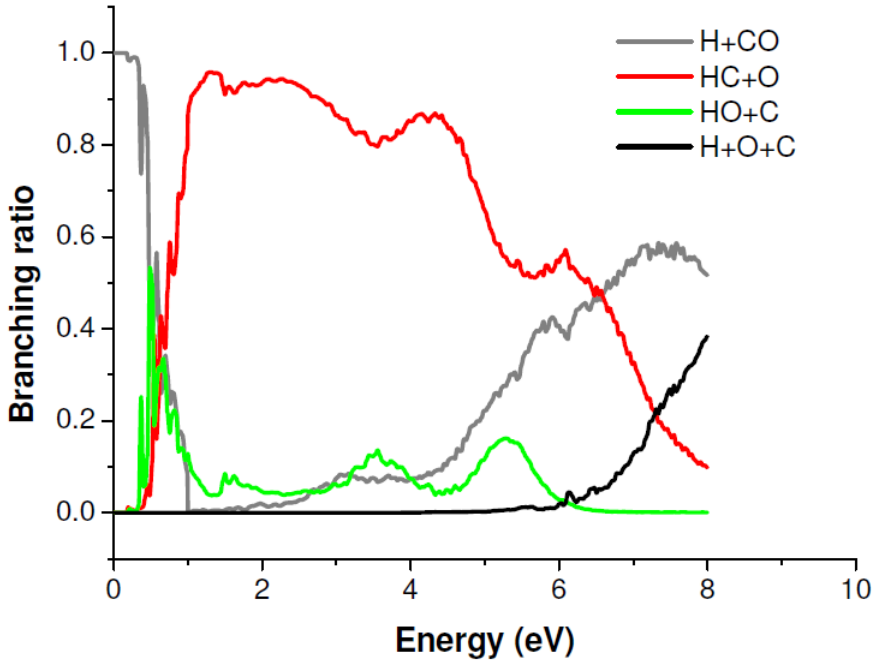

Figure 3.9: *Simulation of the branching ratio evolution on the basis of the calculated resonant states assuming a constant ratio between the two isomers. [3]*

tation channels. The energy range starts at zero relative electron-ion collision energy and ends at 8 eV. The branching into a certain channel gains importance if a corresponding resonant state, which preferentially leads to the dissociation into the regarded recombination products, becomes energetically accessible. The initially dominating branching into the channel comprising the proton and carbon monoxide decreases with increasing detuning energy as consequence of the rise in the other two-body channels. The latter show clear structures according to the position of the resonant states calculated for HCO and HOC. These are lower in energy for the isoformyl cation, which is the only precursor for a fragmentation into HO and C. Consequently the branching into this channel becomes relevant already for lower energies than the branching into the HC + O channel. This channel opens later, adopts the role of the dominating channel and shows a sustained maximum occurring because a dense series of resonant states of different symmetries lying in the energy interval, over which the maximum lasts. Precondition for the three-body channel is a potential energy surface with repulsive character for both coordinates of the system. The required electronic resonant states occur for Δ symmetry of the system at relatively high energy values in accordance to the delayed rise of the three-body channel. The simulation is only based on the calculated resonant states. It does not imply any further electronic states above the calculated lowest ones and consequently is not neces-

sarily significant for detuning energies above the energy positions of the calculated states. A comparison between the simulated and the measured branching-ratio evolution will be given in section 5.3.

4. Molecular fragmentation study

Storage ring experiments, which apply the merged-beam technique, have proven to be a powerful investigation method for the dissociative recombination of molecular ions with electrons. The molecular ion beam is aligned with an electron beam of variable energy giving the possibility to perform measurements at different relative electron-ion collision energies, which will be also referred to as detuning energies in the following. The fragmentation of the molecular ion is initiated by an electron capture. The resulting neutral fragments are not affected by the magnetic lattice of the storage ring and enter a neutral fragment beamline, at which the detector is installed.

The molecular fragmentation study has been performed at the heavy-ion storage ring TSR at the Max-Planck-Institute for Nuclear Physics in Heidelberg. Figure 4.1 shows a schematic view of the TSR declaring the source and the detector as the decisive setup components beside the storage ring itself. The dipole magnets which guide the ion beam are displayed. The focusing quadrupole magnets are not shown for the purpose of clearness. The test storage ring is described in detail in [17]. The features of the source and the capabilities of the detector have the strongest influence on the measurement results and have to be taken into account for any following interpretation. They are dealt with in section 4.2.

The use of the deuterated variant of formyl cations avoids the problems arising if too light fragments occur in the fragmentation channels. Their kinetic energy after the dissociation is proportional to their mass. The detection of the particles requires a minimum kinetic energy and therefore the single recombination products should be chosen to be as heavy as possible.

A previous isomeric relaxation study [7] and its importance to the present experiment are presented in the first section 4.1. Finally a critical discussion of the problematic aspects of the data analysis will be given in section 4.3.

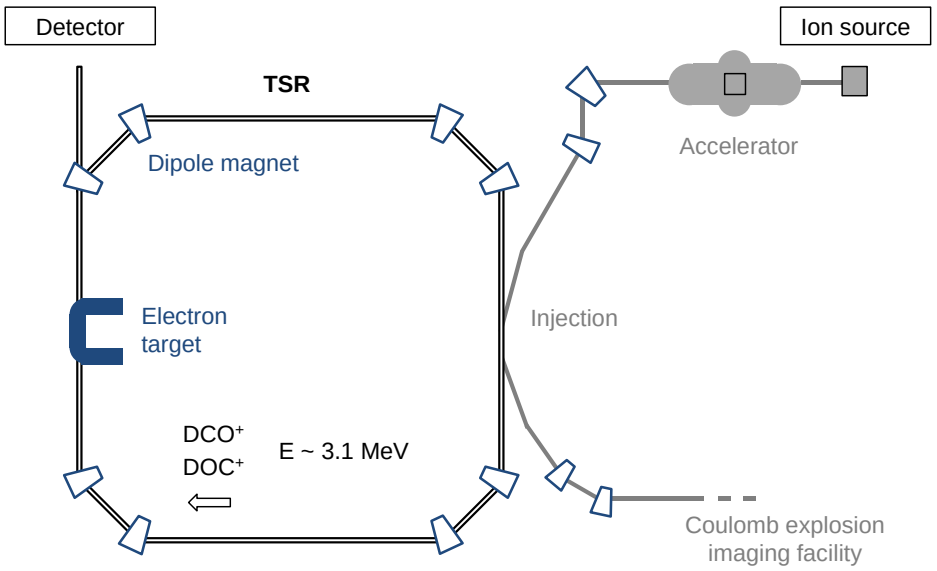

Figure 4.1: *Schematic view of the heavy ion storage ring TSR including the ion source, the detector and the Coulomb explosion imaging facility. The quadrupole magnets, which are used to focus the ion beam, are not displayed for the purpose of clearness.*

4.1 Previous isomeric relaxation study

In the run-up to the experiment focusing on the investigation of the dissociative recombination an independent study of the relaxation dynamics of the isomeric system DCO^+/DOC^+ [7] has been performed, which has a preliminary character for the present molecular fragmentation study.

The vibrational relaxation due to spontaneous radiative transitions as a function of the storage time and the possibility of isomerization of deuterated formyl and isoformyl cations have been probed at the TSR under identical systematic conditions providing elementary information for the interpretation of the measurement data. In this preliminary experiment the foil-induced Coulomb explosion of the molecular ions has been analyzed using three-dimensional coincident fragment imaging.

The molecular ions have been stored in the storage ring for different time intervals corresponding to different degrees of internal relaxation and guided to the fragment beamline at which the Coulomb explosion imaging facility is set up. Figure 4.1 includes the loca-

tion of this facility. Penetrating a thin foil mounted in front of the 3D imaging detector most of the electrons are removed rapidly from the molecule and the dynamics of the remaining ions is determined by the repelling Coulomb potential. Since the motion of the nuclei only negligibly is affected by scattering from the target atoms in the foil, the spatial structure of the molecules can be imaged by measuring the asymptotic velocities of all ionic fragments by coincidence imaging. The measured structure distributions are compared to theoretical distributions, which are derived with the help of vibrational wave functions. This enables to extract the relative population of excited vibrational states. A detailed description of the Coulomb explosion imaging technique is given in [18].
The results of the relaxation study of the isomeric system are summarized in [7]. Concerning the present study there are two remarkable findings.

1. No isomerization of low-lying vibrational levels of DOC^+ has been monitored. This is in accordance to theoretical calculations [6] expecting isomerization processes only for extremely high excited vibrational levels, which are situated less than 120 meV under the barrier to isomerization (see figure 2.2 in section 2.1).

   Under storage ring conditions such high excitations can be excluded. The lifetime of the metastable isomer against isomerization into the energetically favored configuration has been estimated to be larger than 60 s, which clearly exceeds the storage times of approximately 25 s in the present investigation.

   The abundance ratio between the two isomers consequently remains constant. It amounts to $\frac{[DCO^+]}{[DOC^+]} \approx 9$.

2. While the stretching modes of the deuterated formyl cation and its isomeric variant thermalize within several milliseconds with the 300 K background radiation field, the bending mode of the system is excited even after 12 s of storage time. The average bending vibrational quantum number for DCO^+ amounts to $\nu_2 = 3$.

4.2 Experimental procedure

The experimental procedure can be subdivided into three main sequences, which are covered by the three following subsections. The deuterated formyl cations are produced in a fragmentation process. In the consecutive step they are guided to the storage ring and during their storage time cooled with the help of the electron target. The final step comprises the detection of the neutral recombination products. Their impact positions and the respective masses are identified and the fragmentation channel is assigned.

The measurements are distinguished according to the fact whether they have been performed at zero detuning energy or by successively increasing the relative electron-ion collision energy. In the latter case of energy scans there are two modes. In the cooling mode the electron velocity is matched to the ion beam velocity to assure an efficient cooling. The measurement mode is characterized by an elevation of the electron energy to the required parameter for the detuning energy. Both types of measurement start with a precooling sequence.

4.2.1 Ion beam generation

The production and the acceleration of the deuterated formyl cations proceed simultaneously. A cesium sputter source is employed to generate deuterated methoxide anions CD_3O^-. These are used as precursor and accelerated towards the high voltage terminal of a Tandem van-de-Graaff accelerator, at which a nitrogen gas target is installed, gaining a kinetic energy of 1.67 MeV. In a fragmentation process the precursor anions do not only loose electrons but also nuclear compounds resulting in the production of lighter positively charged ions. The positive ions are accelerated in a second acceleration phase towards the final energy of 3.16 MeV and mass selected using a magnetic dipole field before they are injected into the storage ring. The main parts of the experimental setup for the beam preparation are shown schematically in figure 4.2.
Resorting to the preliminary relaxation study 4.1, in which it has been monitored that on one side there is a fraction of DOC^+ ions in the beam but on the other side no isomerization is expected, this fraction consequently is generated in the source during the fragmentation process. Most likely a rapid isomerization from highly excited DCO^+ ions immediately after the collision process with the nitrogen atoms result in the change of the molecule configuration. Based on the calculations referred to in section 2.1 a lower limit for the inner excitation of the deuterated formyl cations can be estimated. An isomerization is possible exclusively for states lying at least 3.21 eV above the electronical ground state.
The low abundance ratio of the isomeric variant is a consequence of the molecular structure of the precursor anion. The deuterated formyl cations are produced preferentially since the configuration of CD_3O^- comprises three D-C bonds and no D-O bond which is a precondition for the DOC^+ configuration.

4.2.2 Storage of molecular ions

After the injection into the heavy-ion storage ring TSR the molecular ion beam is phase-space cooled and the molecular ions are vibrationally cooled with the help of an electron

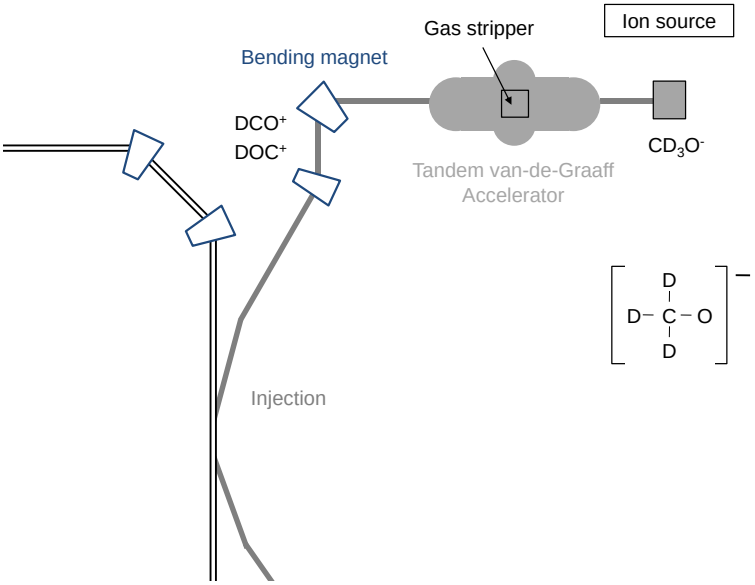

Figure 4.2: *Experimental setup for the beam preparation including the cesium sputter source, the tandem accelerator and the dipole magnets for mass selection and injection into the storage ring. The structure of the deuterated methoxide anions is displayed additionally.*

cooler, which is employed as electron target in the measurement mode of the experiment. Within the overlap region of the two beams the Coulomb interaction between the ions and the electrons lead to a frictional force that adapts the ion velocity to the electron velocity reducing the momentum spread of the stored beam. Moreover the divergence and the cross-sectional area of the beam are decreased.

Performing energy scans the energy and thus the velocity of the electrons is altered worsening the cooling conditions. For this type of measurements time intervals exist in which the electron velocity is set to the cooling value. These time intervals form the cooling mode assuring a continued cooling. The abundance ratio between the two isomers remains constant during storage time because no isomerization is expected (see section 4.1). For cooling purposes the ions are stored for time intervals ranging from 6 up to 10 s in the precooling step.

The dissociative recombination is initiated and proceeds within the $L = 115(1)$cm long overlap region of the ion and the electron beam. The initially positively charged molecules are neutralized and dissociate. The recombination products also are neutral and are not affected by the magnetic fields of the focusing and bending magnets. They enter the neutral fragment beamline, at which the energy-sensitive imaging detector is installed. The distance between the center of the electron target and the detector amounts to $D = 941(1)$cm. The positions of the electron target and the neutral fragment beamline are

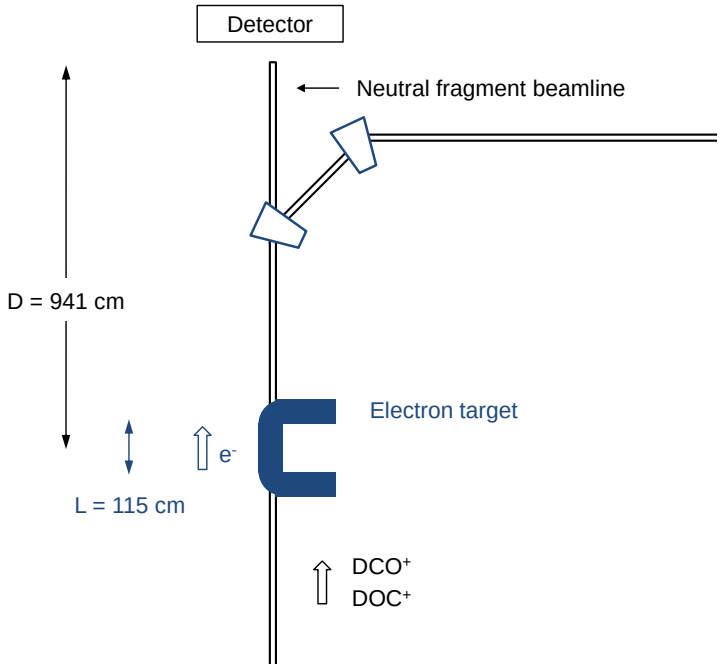

Figure 4.3: *Schematic view of the positions of the electron target and the detector system. There is no clear definition of an interaction point along the L = 115(1)cm long overlap region. The distance between the center position of this overlap region and the detector surface amounts to D = 941(1)cm.*

displayed in figure 4.3.
The merged-beam technique enables to perform measurements at freely adjustable relative energies between electrons and ions by altering the electron acceleration voltage of the electron target. However there is no strict definition of an interaction point, which complicates the analysis of the recorded data. The formulation of the problem arising from this fact and its solution are considered in section 4.3.1.

4.2.3 Energy-sensitive imaging detector

The detector system installed at the neutral fragment beamline has been designed and developed primarily in order to measure the branching ratios into the different accessible fragmentation channels. It is capable of recording multi-fragment events, following the dissociative recombination, by coincidence imaging and capable of a simultaneous identification of the recombination products by their masses. A schematic view of the detector system is displayed in figure 4.4.
Originating from the interaction region in the electron target the neutral recombination products enter the setup from the left. The shutter protects the detector during the

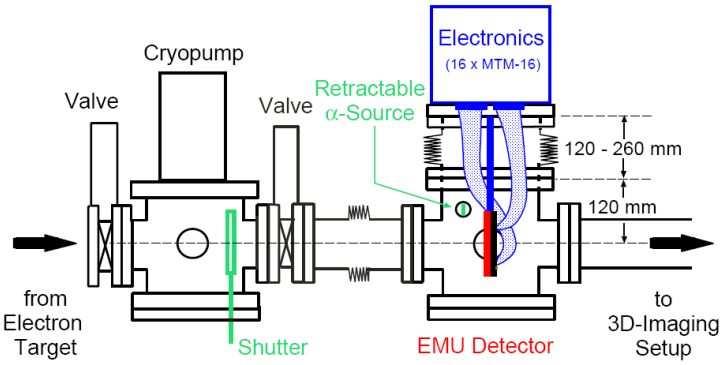

Figure 4.4: *Schematic view of the detector system installed at the neutral fragment beamline. The recombination products enter from the left side. A shutter protects the detector during injection. The retractable α-source is used for offline tests. The electronics of the detector system are located outside of the vacuum. The detector can be retracted to enable a use of detectors which have a larger distance to the electron target. [19]*

injection phases. The retractable α-source can be shifted and located in opposite to any region of the detector surface. It serves offline test and calibration purposes. The imaging detector is mounted in a large bellow and can be retracted in order to switch to detector systems installed in the beamline at larger distances with respect to the electron target. Under running conditions the vacuum in the detector chamber amounts to 5×10^{-9} mbar. A description of the electronic setup of the detector system is given in [19]. With the current settings count rates of 2 kHz can be achieved.

The main component of the detector system is the energy-sensitive imaging detector named EMU. The EMU detector is a surface barrier detector, which is upgraded by a special strip structure on its frontside (junction side) and its backside (ohmic side). The abbreviation EMU refers to this strip structure meaning Energy-sensitive MUlti-strip detector. A schematic cross section through the EMU detector is displayed in figure 4.5.

The surface barrier detector is a 97.3 mm $\times$ 97.3 mm large silicon crystal and 300 μm thick. Its front-side active area is subdivided into 128 vertical strips of 730 μm width, which are separated by gaps of 30 μm width. The backside is separated analogously in 128 horizontally aligned strips with slightly modified strip and gap widths of 700 μm and 60 μm, respectively. Each of the strips consists of two layers. The upper layer meets the technical requirements of undisturbed signal transmission to the laterally attached readout electronics. It is made of aluminum and 100 nm thick. The second layer is made of doped silicon (p^+ Si), 100 nm thick and embedded into the 300 μm thick silicon main component of the detector creating a semiconductor junction thereby. At this interface a

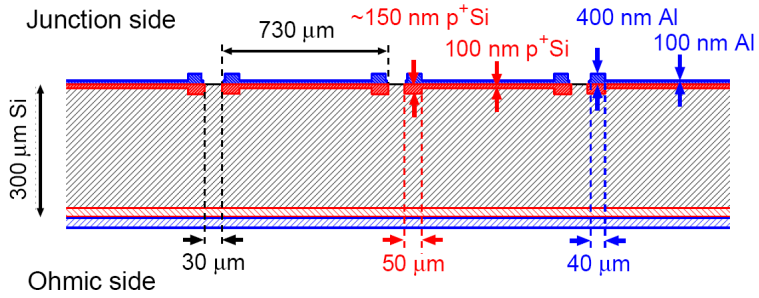

Figure 4.5: *Schematic cross section through the EMU detector. The two layers of the single strips are made of aluminum and doped silicon, respectively. There will be no responding strip if particles hit the gap regions. The signal current is lower if particles loose energy in thicker areas on the strip edges before they enter the junction. [19]*

depletion zone is formed, which do not contain any mobile charge carriers. The depletion zone is extended over the entire detector depth by applying a reverse-bias voltage of 70 V. The strip edges of both layers have an increased thickness, by which the single strips can be clearly differentiated. The subdivisions of both detector sides represent the realization of the position sensitivity since they enable a stripwise readout of the signals created by incoming particles.

The neutral particles impinging on the detector create electron-hole pairs in the semiconductor junction, whose number is proportional to the energy the particles loose on their trajectory within the detector. The generated electron-hole pairs are collected by an electric field forming a current signal. Since the mean free path of the particles in the detector is decisively smaller than the active detector depth a complete deposition of the particle energies occurs. Consequently the created current signal is proportional to the kinetic energy. Thus the surface barrier detector is energy-sensitive regarding every single strip in addition to its position sensitivity.

The energy sensitivity corresponds to mass sensitivity. Regarding the kinetic energy of the initially stored particles E_{kin} the release energies occurring in the dissociative recombination E_{KER} are negligibly small showing a difference of five orders of magnitude $\frac{E_{KER}}{E_{kin}} \sim 10^{-5}$. Consequently the recombination products propagate with nearly the same velocity after the dissociation of the recombined molecule. Their difference in mass therefore is reflected by the difference in their kinetic energy, which can be measured by the detector.

For the purpose of a short recapitulation figure 4.6 illustrates the concept of the detection utilizing the EMU detector system.

An initially positively charged particle captures an electron, forming an unstable neutral

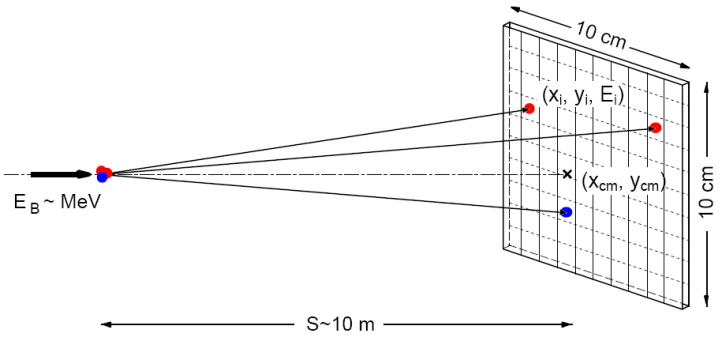

Figure 4.6: *Concept of the detection using the double-sided fully-depleted surface barrier detector system EMU. The signals created by the single neutral fragments are proportional to their mass. Their stripwise readout enables to reconstruct the pattern of the impact positions. The cross on the detector surface denotes the center-of-mass position of the event. [19]*

state, which stabilizes through dissociation into neutral fragments. The velocities of the recombination products correspond to the velocity of the dissociating molecule and they are only negligibly altered due to the kinetic energy release occurring during the dissociative recombination. The fragment masses consequently determine the kinetic energy of the single neutral particles propagating towards the detector. The particles hit the strips of the detector creating signal currents, which can be readout individually for every strip, proportional to their mass. Recording the mass- and position-information on an event-by-event basis by coincidence imaging the breakup can be uniquely identified and assigned to one of the possible fragmentation channels. Ambiguities in the event reconstruction cannot be excluded since the readout is only possible for the single strips but not for each of their overlap regions. Analyzing the measurement data, these ambiguities are taken into account. This subject solely is a problem of recording data and will not be discussed within the scope of this thesis. A detailed discussion is given in [20].

4.3 Analysis

A typical pulse height spectrum recorded during the measurements of the dissociative recombination of deuterated formyl cations is displayed in figure 4.7.
The vertical lines mark the limits of the mass windows which are set to classify the pulse heights and assign them to the fragment masses. The peak on the left side occurs due to background events. It is strongly suppressed by the adjustment of a threshold for the signal record.
Figure 4.8 displays the center-of-mass distribution of the recorded events in x- and y-

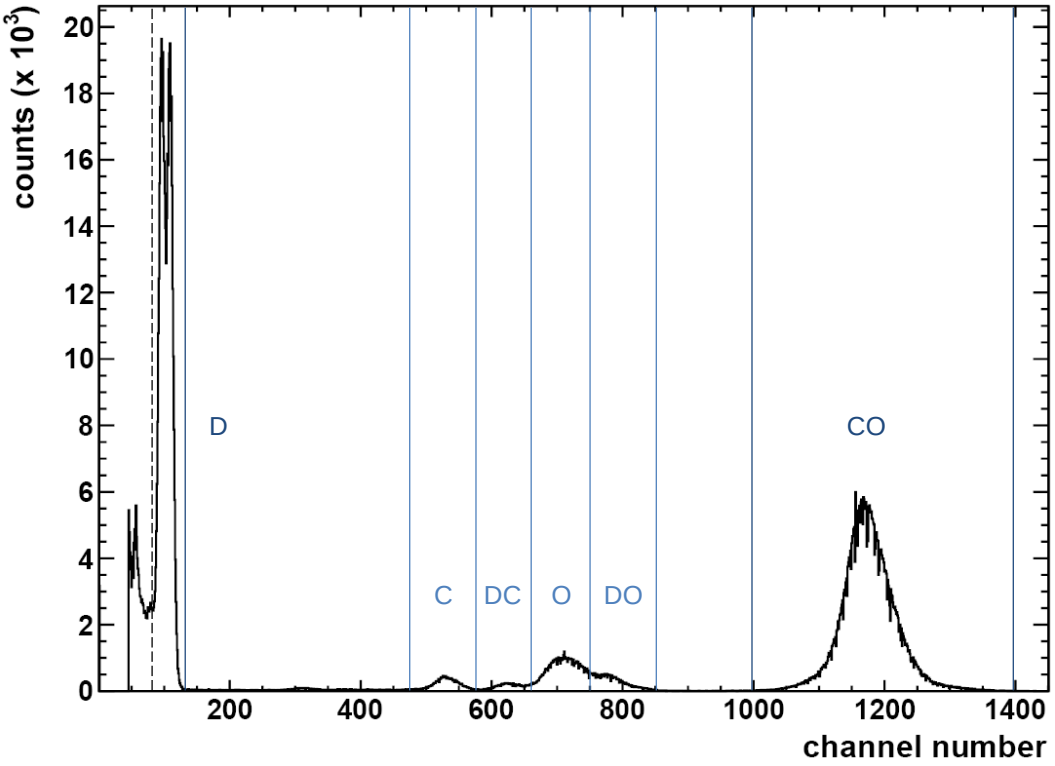

Figure 4.7: *Representative pulse height spectrum at zero detuning energy summed over all strips on the front side. The events are measured by coincidence imaging and thus the fragmentation channels can be assigned on an event-by-event basis. The dashed line represents the threshold for the detection. The solid vertical lines define windows for particle identification by their masses. The corresponding recombination products are assigned.*

direction. Based on these plots the center position of the beam and the variances σ of the two Gaussian profiles are determined. The latter allow to perform σ-cuts on the center-of-mass position, which reduce the influence of background events directing the focus to the events whose center-of-mass lie within a limited circle area around the beam center position. Events with a center-of-mass outside of this defined area are not considered in the analysis. The small variances of the curves are the result of the efficient cooling of the beam.

The inner excitation of the molecular recombination products can be extracted from the projected fragment distance distribution. The exact analysis procedure is dealt with in section 5.1.1. The required distribution is obtained calculating the distance between the impact positions of the fragments in the detector plane. In order to determine the branching ratios the events, which has been recorded and identified with the help of the EMU detector, has to be counted.

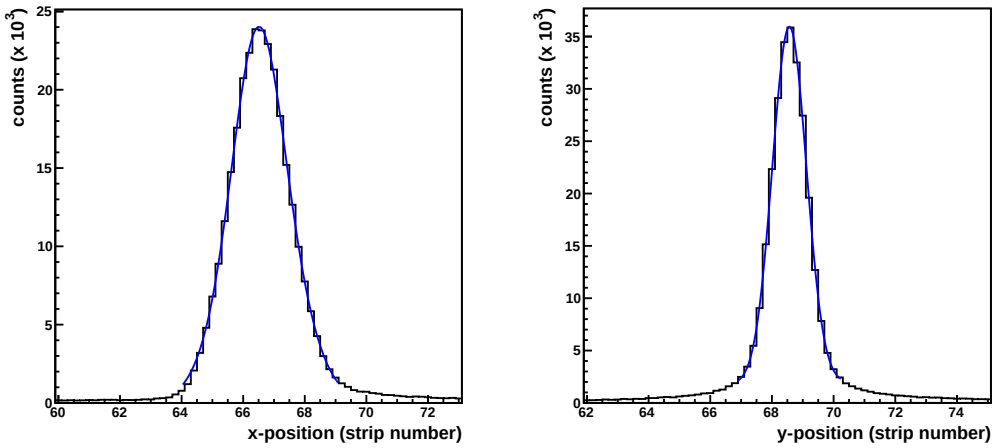

Figure 4.8: *Center-of-mass distributions in x- and y-direction. The Gaussians are fitted to the histograms in order to determine the center-of-mass positions and their variances.*

The analysis is complicated mainly because of three aspects.

1. Errors in event reconstructions cannot be excluded due to an ambiguous signal record.

2. Events resulting from background processes obscure the recombination signal.

3. Depending on the fragmentation channel the detection efficiency is reduced due to the finite detector size, the strip structure and the geometry of the experimental setup.

The first aspect takes into account, that particles impinging on the detector may hit a gap region or a region with increased thickness on one of the strip edges. In the first case there will be no responding strip. In the second case the signal current will be lower because the particle has lost energy penetrating the thicker entrance window. All effects caused by the ambiguous stripwise readout and possible special fragment trajectories are corrected for by a Monte-Carlo simulation discussed in the first subsection.
The subject of the second subsection is the background estimation for zero relative electron-ion collision energy and for elevated detuning energies.
Furthermore the kinetic energy release of the fragmentation channel containing deuterium, which is the lightest fragment occurring in the dissociative recombination of deuterated formyl cations, and carbon monoxide is large enough to imply the possibility that the deuterium atom passes the detector because the transversal velocity component is too

large. An estimation of the error caused by this possible loss of particles will be discussed in the third subsection.

4.3.1 Monte-Carlo Simulation

The analysis of the recorded data requires employing a Monte-Carlo simulation of the dissociation process, the subsequent propagation of the fragments towards the detector and the detection procedure. The simulation enables to cope with the missing information about the actual position of the molecule fragmentation and the orientation of the molecular ion as well as the possibility that recombination products from a given fragmentation channel may create misleading signals during the detection process depending on the detector surface structures and their hit pattern on the detector, which itself again changes according to the exact position of the breakup.
These problems cannot be solved for a single event. However they can be dealt with using statistical methods under the assumptions that the position of the dissociation initiation along the overlap region of the electron and the ion beam and the orientation of the deuterated formyl cations relative the ion beam direction are uniformly distributed. These assumptions are acceptable since there are no reasons why a particular breakup position or a special molecule orientation should be favored.
The focus of the analysis is not on the descriptions of the dissociative recombination of a single molecule but on the features of this molecular process regarding particle ensembles. This focus declaration enables to employ statistical methods and to avoid the following problematic aspects of the analysis.

1. The distribution of the projected fragment distances essentially depends on the two parameters outlined above. Observing an ensemble of particles the Monte-Carlo simulation is employed to solve the problem of the missing information about the concrete interaction point and the molecular orientation with the help of the statistical methods.

   For the analysis regarding the inner excitation of the molecular fragments the simulation is carried out for different energy parameters, which define the kinetic energy available for the recombination products. In a subsequent step theoretical distributions for the projected fragment distances are extracted from the simulation results, which serve as fit parameters in the following analysis. The integration of the simulation results into the analysis is discussed in section 5.1.1.

2. The detector efficiency is determined by its strip structure. Since the fragmentation

[%]	D + CO	DC + O	DO + C	D + C + O
D + CO	99.14	0	0	0.86
DC + O	0	99.14	0	0.86
DO + C	0	0	99.93	0.07
D + C + O	0.05	0.20	0.38	99.37

Table 4.1: *Simulation of the branching ratios allowing only the fragmentation into the channel defined in the first column. Exemplarily the simulation of the (D+CO)-channel additionally yield a small branching into the three-body-channel. The detector efficiency is slightly altered for the four accessible fragmentation channels.*

channels differ from each other in the number and the structure of the recombination products it cannot be excluded, that the probabilities for detection are slightly different for the various channels. Moreover occasionally signals may be generated which indicate a different fragmentation channel because particles impinge on gap regions or regions with an increased thickness. Due to these possible misinterpretations the measured branching ratios consequently may not reflect the real branching ratios.

The simulation takes into account the geometry of the entire experimental setup and considers the detector status. The dissociation of each of the four fragmentation channels have been simulated independently for a sufficiently large number of events. Table 4.1 summarizes the results of these simulations.

The information obtained by this method are translated into a (4×4)-matrix. Having inverted and normalized this matrix into the correction matrix C the real branching ratios can be derived performing the following calculation.

$$\vec{v}_{real} = C \cdot \vec{v}_{measured}$$

In this presentation the vectors $\vec{v}_{real}$ and $\vec{v}_{measured}$ are composed of the four actual and measured branching ratio values, respectively. Matrix C has the following components.

$$C = \begin{pmatrix} 1.006 & -0.009 & -0.001 & -0.009 \\ -0.001 & 1.009 & 0 & 0 \\ -0.004 & 0 & 1.001 & 0 \\ -0.002 & 0 & 0 & 1.009 \end{pmatrix}$$

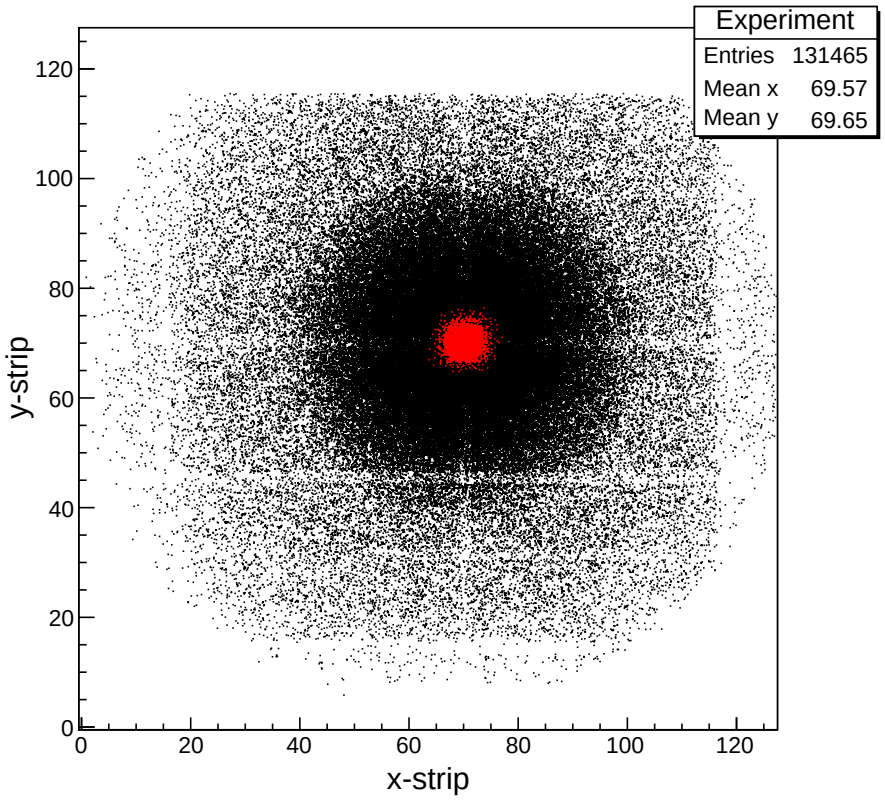

Figure 4.9: *Impact positions of deuterium (black) and carbon monoxide (red) on the detector surface. The symmetric cross structure is a consequence of the assignment procedure of the event identification. The effect of the defect horizontal strip is clearly visible. The active detector area corresponds to the entire square.*

Because of its far-reaching influence on the final results of the experiment the Monte-Carlo simulation is cross-checked probing the distribution of the impact positions on the detector surface for the (D+CO)-channel. Figure 4.9 displays this distribution obtained in the measurement.

The active detector area corresponds to the entire square. Resulting from an isotropic dissociation process the impact positions of both recombination products lie within a circle. For carbon monoxide the red position markers obviously reflect this structure on the detector surface. In the case of the black markers displaying the positions for the deuterons the rough circular structure also is recognizable. It is modified due to the setup features. The horizontal cuts at the top and the bottom of the circle result from a particle loss at the position of a dipole magnet which prevents a further propagation of the particles. Besides the 46^{th} horizontal strip was defect during the measurement. The number of detected particles decisively is reduced along this strip. The cross structure centered at the center-of-mass which is superimposed on the position distribution occurs

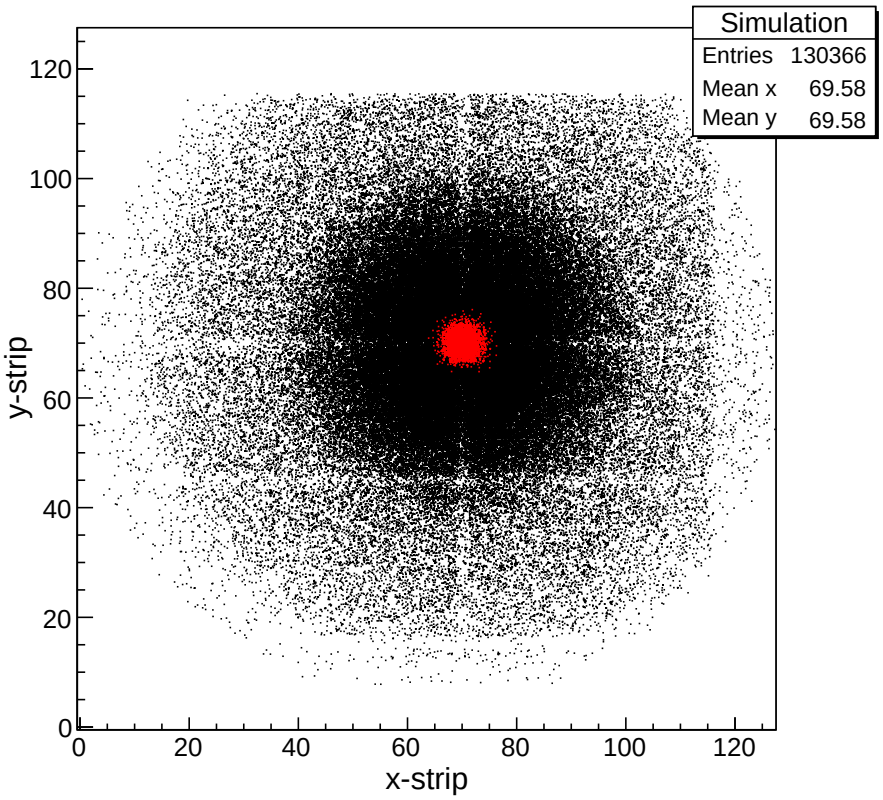

Figure 4.10: *The simulation of the particle propagation is in convincing agreement with the measurement data. The maximum radius of the complete pattern, the cross structure and the defect strip are reproduced in a representative way.*

because of the interpretation of the signals obtained in the measurement. It does not affect the experimental results. A discussion of this latter feature is given in [20].
The simulated distribution of the impact positions of the particles is shown in figure 4.10. Every aspect observed in figure 4.9 is reflected by the theoretically obtained position distribution. The simulation thus describes the actual systematic conditions of the experiment accurately.

4.3.2 Background estimation

The influence of background events predominantly caused by restgas collisions will be estimated within this subsection. For this particular analysis two circular reference areas are defined on the detector surface. The first area A_{center} is centered at the center-of-mass position of the ion beam. It contains the center-of-mass positions of events, which originate from dissociative recombination or restgas collisions. The second area A_{side} comprises the events recorded in a side peak, which exclusively contains events not

Channel	Branching ratio [%]
D+CO	91.9 ± 0.9
DC+O	2.6 ± 0.1
DO+C	0.7 ± 0.1
D+C+O	4.8 ± 0.7

Table 4.2: *Branching ratios of the background measurement. The values have been corrected using the correction matrix. The dissociation into the (D+CO)-channel is clearly dominating.*

resulting from dissociative recombination.

Investigating the measurement results obtained in a background run, in which the electron-beam has been switched off during measurement mode, the ratio between the number of events in both areas has been determined to be $\frac{N_{center}}{N_{side}} = 1.727$. N_{center} refers to the number of events detected in the center area A_{center} and N_{side} correspondingly to the number of events in the side area A_{side}.

Resorting to this ratio $R = \left[\frac{N_{center}}{N_{side}}\right]_{background}$ it is possible in a very accurate approximation to estimate the number of events, which are not caused by dissociative recombination, in the center area A_{center} by counting the events recorded in the side area A_{side} under the assumption that the derived ratio is constant.

Furthermore the analysis of the background run yields the branching ratios for the non electron-initiated dissociation process. The values, which have been corrected for possible misinterpretations due to misleading detection signals by using the correction matrix derived in section 4.3.1 are given in table 4.2.

The fragmentation into the only exoergic fragmentation channel accessible for deuterated formyl cations dominates. The contributions of the other channels are decisively smaller, whereas the branching into the second exoergic channel (DO+C) is unexpectedly low.

In the following the questions will be answered, whether these background events falsify the interpretation of the experiment and how the recorded data can be corrected for this. The definition of the two reference areas A_{center} and A_{side} enables to determine the ratio, in accordance to the calculation of the ratio for background run, for measurements performed at arbitrary relative electron-ion collision energies. The events in both areas are counted and their total numbers N_{center} and N_{side} are divided. Figure 4.11 displays the ratio as a function of the detuning energy E_{cm}.

The dashed line represents the ratio R determined in the analysis of the background run. At zero detuning energy the number of events in the center area N_{center} approximately

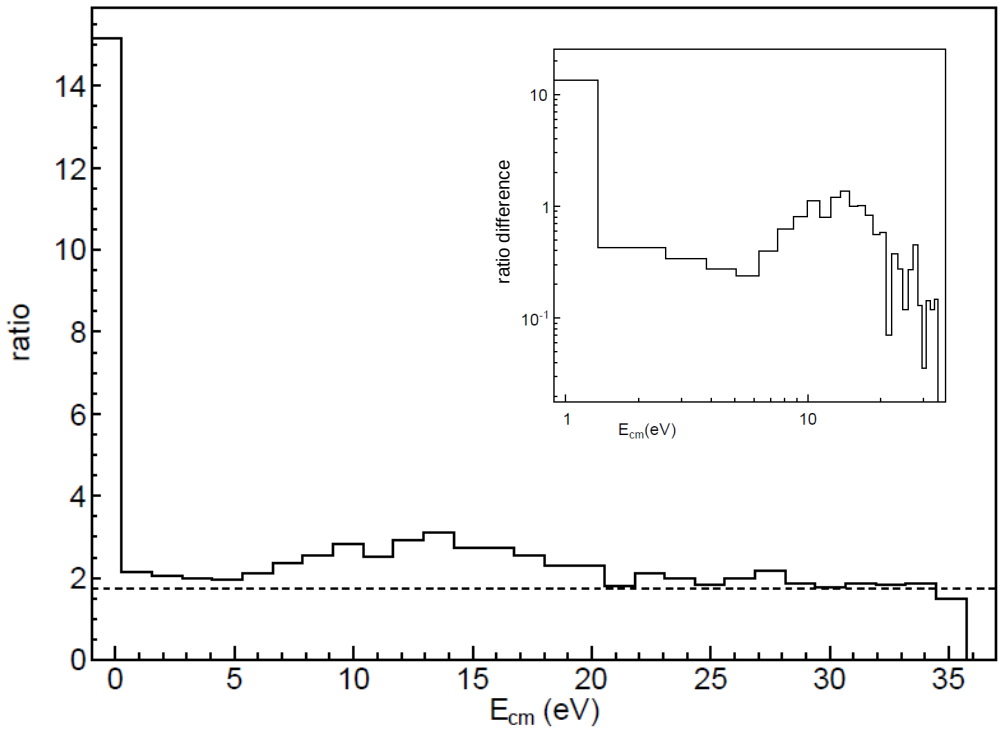

Figure 4.11: *The ratio between the counts in the defined center area and the counts in the side area. The dashed line represents the background measurement ratio. The plot conveys an idea of the evolution of the energy dependent cross section for dissociative recombination. The insert shows the difference between the ratio obtained in the energy scans and the background measurement ratio as a function of the detuning energy using logarithmic scales.*

is 15 times higher than in the side area. A correction for this small contribution from background events is not necessary.

However for elevated detuning energies the ratio is close to the background ratio R indicating that events originating from restgas collisions obscure the events resulting from electron capture induced dissociative recombination. The determined ratio is situated above the background ratio with one exception at the maximum detuning energy. Consequently there is a contribution from dissociative-recombination events. For the purpose of a detailed analysis the data has to be corrected for these superimposed background events.

The insert in figure 4.11 shows the energy dependent evolution of the difference between the ratio obtained in the energy scans and the background measurement ratio. It conveys an idea of the dependence of the cross section for dissociative recombination on the detuning energy.

Regarding the analysis of the inner excitation for elevated detuning energies a correction is not possible because the distribution of the projected fragment distances has to be known for the background run. In this case the background contribution is dealt with differently, as will be discussed in 5.1.2.
Since no additional information concerning the background events are required in the case of the branching-ratio analysis the subtraction of the background contribution is performed to obtain the real energy dependent evolution. The number of events in the side area A_{side} is counted separately for each detuning energy and subtracted from the counts N_{center} in the center area having been scaled with the determined background ratio R.
Following this train of thought the number of dissociative-recombination events at the detuning energy E_{cm} amounts to

$$N_{DR(E_{cm})} = N_{center(E_{cm})} - c \cdot R \cdot N_{side(E_{cm})}$$

Based on the quantities $N_{DR(E_{cm})}$ the branching ratios are determined for the different channels. The variable c is introduced to correct for a possible background overestimation. The outlined method has the disadvantage that the ratio R is determined under different systematic conditions, since the electron beam is switched off. Figure 4.11 clearly shows that there is a contribution from dissociative recombination. Consequently c has to be chosen from a parameter interval containing values which assure that $N_{DR(E_{cm})} > 0$ independently of the energy. The effect of the choice of c is illustrated in figure 4.12.
The upper curve displays the measured branching ratio exemplarily for the (D+CO)-channel without background subtraction. In this case c equals to zero. For the curves situated beneath the first one c amounts to 0.1 and 0.17, which means that 10% and 17% of the number of background events are subtracted, respectively. The rough curve structure is preserved under background subtraction. The positions of the extrema are the same, although their unambiguous identification has become complicated for the lowest curve. However there is a significant shift in the absolute positions of the curves. Without background subtraction the minimum m of the first curve in the interval 14 eV $\leq E_{cm} \leq$ 15 eV amounts to $m_1 \approx 44$ %. An analysis of the other curves yields $m_2 \approx 28$ % and $m_3 \approx 9$ %, respectively. Since the background influence on the (D+CO)-channel is the strongest one compared to the three other channels the shift of their absolute position is not that considerable.
Nevertheless it is advisable to avoid the term 'branching ratio' in this context and to use 'relative contribution' instead. The branching ratios cannot be stated having performed the parameter-dependent background subtraction. Their relative position and especially

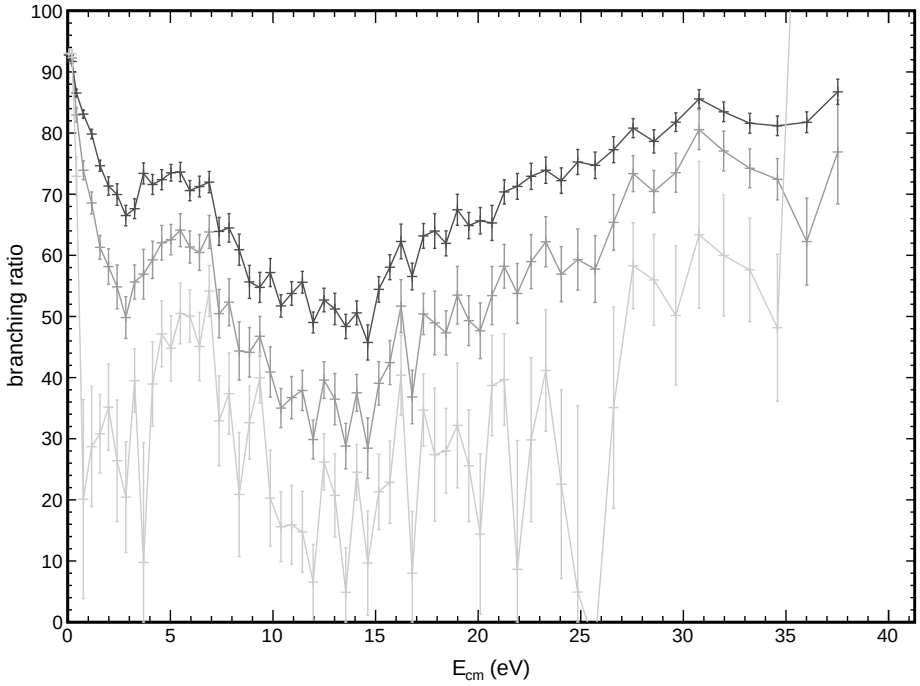

Figure 4.12: *Evolution of the branching ratio into the (D+CO)-channel for three different choices of the parameter c. The upper curve represents the raw measurement data. There is no background subtraction and c amounts to zero. For the two lower curves c amounts to 0.1 and 0.17, respectively. The evolutions of the three plots show comparable structures independently of the amount of subtracted background. The absolute value is determined by the amount of background subtraction and cannot be extracted from the measurement data.*

the qualitative significance however are maintained independently of the choice of c.

4.3.3 Estimation of particle loss due to the setup geometry

Recombination products which take over a high amount of the energy released in the dissociative recombination pass the detector if they gain a sufficiently large transversal velocity component. The loss of these particles lead to an incomplete detection and the events the particles resulted from cannot be reconstructed. The effects on the experimental results arising from this particle loss due to the setup geometry are estimated within this section.

Using figure 4.13, which shows a schematic view on the kinematics of the particles, the possibility of a particle loss is discussed.

The recombination products propagate in z-direction. Their time-of-flight is determined

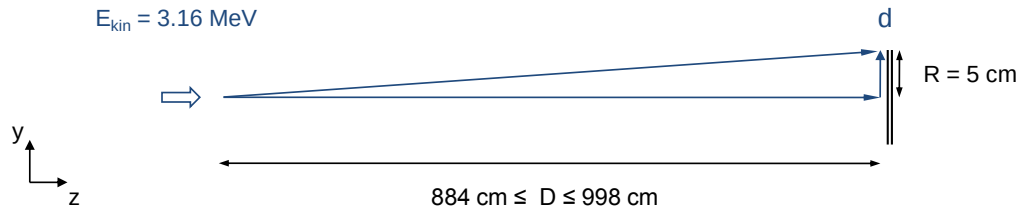

Figure 4.13: *Schematic view on the kinematics of the particles. Since the overlap region covers a distance of $L = 115$ cm the distances D from the interaction points to the detector surface lie within the interval between $D_{min} = 884$ cm and $D_{max} = 998$ cm. If the distance d, which measures the particle propagation in y-direction during their time-of-flight to the detector, extends the detector dimension R a particle loss is expected.*

by their velocity, which corresponds to the velocity of the initial molecular ions given by the molecule mass and the beam energy E_{kin}. A velocity component exemplarily in y-direction possibly is added to the velocity vector of the fragments during the energy transfer proceeding in the dissociation process. If this additional transversal component is sufficiently large the particles cover a distance d rectangular to the propagation direction which is larger than the detector dimension R.
In order to estimate the probability of a particle loss the distance d has been calculated for two channels under the following assumptions.

1. The dissociation is initiated at the largest possible distance to the detector, which is given at the beginning of the overlap region. According to the values given in section 4.2.2 this distance amounts to $D = 9.98$ m.

2. The energy released in the breakup process E_{KER} completely is transferred into kinetic energy of the recombination products. Any additional detuning energy transferred to the system by the electron also exclusively contributes to this kinetic energy.

3. The two recombination products leave each other back-to-back in y-direction.

These assumptions obviously define the most convenient conditions for a particle loss. Under these conditions the lighter recombination product will miss the detector. Thus the calculations lead to an upper estimation for the distances of the lighter particles covered in y-direction. If the calculated distances d exceed the detector dimension R, a particle loss is expected.

E_{cm}[eV]	D+CO	DC+O
0	5.66	
5	7.35	1.32
10	8.72	1.88
15	9.91	2.31
20	10.97	2.67

Table 4.3: *Distances d [cm] covered by the lighter particles of each channel in y-direction. The values represent an upper estimation. If they exceed the detector dimension of R = 5 cm, a particle loss is expected.*

Based on energy and momentum conservation the following formula is derived. The velocities considered are small enough to carry out classical calculations.

$$d = D\sqrt{\frac{E_{KER}}{E_{kin}}}\sqrt{\frac{m_1 + m_2}{m_1\left(1 + \frac{m_1}{m_2}\right)}}$$

The masses of the particles are given by m_1 and m_2. For the lighter particle with mass m_1 the distance d is obtained. Table 4.3 lists the distances for D and DC in the corresponding channels. In these calculations E_{KER} equals the sum of the characteristic energy release given in section 2.2.2 and the added detuning energy E_{cm}.
The kinetic energy release observed for the two-body breakup into deuterium and carbon monoxide is sufficiently large to lead to a loss of deuterium atoms, because their trajectory might not cross the detector surface due to a too large transversal velocity component. The problem does not occur for the other channel because it comprises particles with comparable masses. In the case of the three-body channel the main amount of the energy, which additionally is transferred to the recombined system by the excess energy of the electron, surrenders to the break of the chemical bonds. The distance values therefore do not need to be calculated.
The relative number of events, which cannot be detected with the present experimental setup probing the dissociative recombination of DCO^+ has been determined experimentally. For this purpose the assumption is made, that every event, in which a single neutral carbon monoxide molecule is detected on the detector, results from a failed detection of a deuteron. However the latter is the case, if the deuterium atom either impinges on a gap region of the detector or if it passes the detector. Thus the experimental determination of the ratio $\frac{[CO]}{[CO]+[D+CO]}$, in which [CO] defines the number of detected CO-events and

E_{cm}[eV]	$\frac{[CO]}{[CO]+[D+CO]}$
0	0.002
4 - 10	0.023
10 - 15	0.024
15 - 20	0.037
20 - 35	0.065

Table 4.4: *Systematic error estimation derived by experimentally probing the number of events for the CO and the (D+CO) detection.*

correspondingly [D+CO] the number of (D+CO)-events, represents an upper limit for the relative amount of (D+CO)-events which are undetectable.
In a reference area corresponding to a 2σ center-of-mass cut the numbers for both events are counted. The results are presented in table 4.4.
The upper limit for the systematic error derived by this method is set to the corresponding values. The other channels are considered to be uncritical with regard to this systematic error. It particularly is taken into account for the determination of the relative contributions discussed in section 5.2.

5. Experimental results

The focus of the interpretation is on the inner excitation of the molecular recombination products and the branching ratios into the different fragmentation channels. The first aspect is determined investigating the projected distance distributions of the recombination products. The single steps of this interpretation are outlined in section 5.1. The second aspect is the main subject of the molecular fragmentation study and the results are presented in the second section 5.2 of this chapter. Both sections are subdivided into two subsections separately dealing with the respective aspect at zero and elevated relative electron-ion collision energy.

5.1 Inner excitation of molecular fragments

The energy balance, which is drawn up in section 2.2.1, is the starting point for the analysis of the inner excitation of the molecular recombination products. Generally speaking a higher amount of kinetic energy release leads to a larger distance between the fragments on the detector. This energy release complements the electronical and rovibrational excitation of the recombination products to the characteristic amount of energy release inherent in the process of dissociative recombination. Performing the analysis the influences of the random molecule orientation prior the dissociation process on the distance distribution are taken into account employing the simulation routine presented in section 4.3.1. Since there is only one exoergic channel, which comprises one molecular recombination product and three characteristic release energies, the inner excitation can be probed at zero detuning energy under unique conditions. This exceptional investigation is discussed in section 5.1.1. The second section deals with the inner excitation at elevated detuning energies. The results for the two two-body channels accessible from the initial molecule DCO^+ are presented.

5.1.1 Inner excitation of carbon monoxide at zero relative electron-ion collision energy

At zero detuning energy there is hardly any effect on the measurement data resulting from the detection of background events as section 4.3.2 has shown. Thus for this special case an investigation of the inner excitation of the molecular recombination product is feasible. Since for DCO^+ only the fragmentation channel which comprises D and CO as recombination products is exoergic, the analysis is restricted to carbon monoxide. A probe of the inner excitation of DC is not possible because the corresponding fragmentation channel is endoergic. The branching ratio into the exoergic channel leading to the production of DO and C is suppressed due to the low abundance of DOC^+ in the beam. For the latter channel the recorded data do not enable a detailed investigation because of insufficient statistics.

The analysis of the inner excitation of carbon monoxide resorts to the simulation 4.3.1 and utilizes a fit of theoretically obtained data to the measurement data. It aims to extract the relative population of the electronical and vibrational states of CO from the normalized projected fragment distance distribution. Since the simulation is implied in the analysis it is possible to conclude the distribution of the amount of kinetic energy released during the dissociative recombination from the measured distance distribution of the particles. The larger the distance of the particles, the more energy has been transferred to the fragments as kinetic energy. The characteristic amounts of the total energy release are known. Following the considerations on the energy balance in section 2.2.1 the difference between this total and the kinetic energy is the energy tranfered to the molecular recombination product leading to an inner excitation.

As a reminder the three possible channels leading to the recombination products in focus are listed.

$$\begin{aligned} DCO^+ + e^- &\longrightarrow CO(X\ ^1\Sigma^+) + D(^2S) + 7.25\ eV \\ &\longrightarrow CO(a\ ^3\Pi_r) + D(^2S) + 1.24\ eV \\ &\longrightarrow CO(a'\ ^3\Sigma^+) + D(^2S) + 0.38\ eV \end{aligned}$$

The two excited electronic states $a\ ^3\Pi_r$ and $a'\ ^3\Sigma^+$ are situated above the ground state of the carbon monoxide molecule $X\ ^1\Sigma^+$. The energy differences between these states correspond to the difference in the amount of released energy, since the lowest excited electronic state for the deuterium cannot be reached by the energy released.

In the following the fundamental aspects of the analysis procedure will be outlined on the

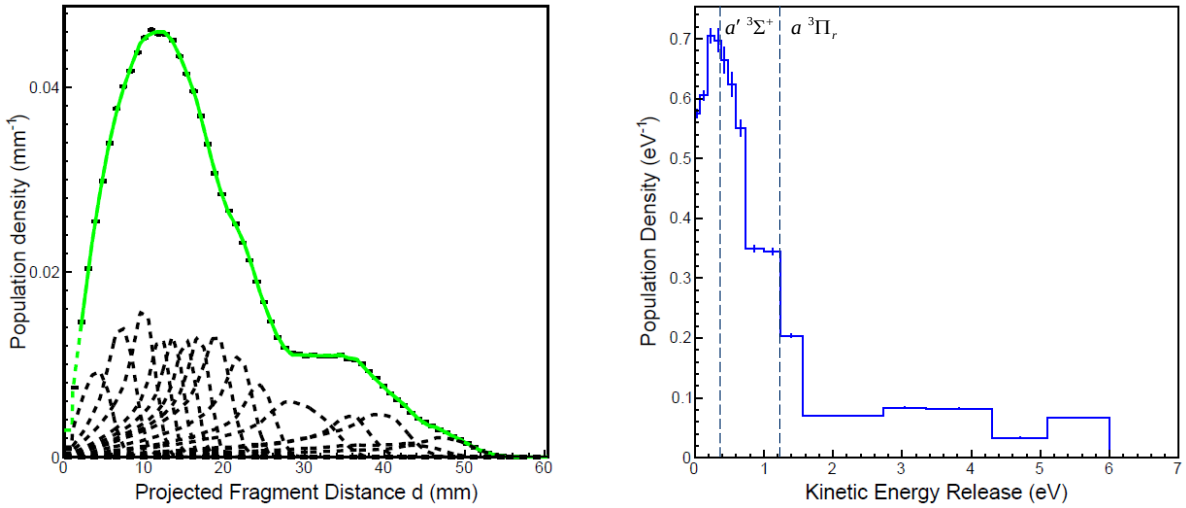

Figure 5.1: *The left plot contains the measurement result and the fit result (green curve) based on the simulated distance distributions, which are represented by the dashed curves. In the right plot the energy intervals serving as input parameters for the simulations and their weights derived by the fit are displayed.*

basis of figure 5.1, which displays two complementary diagrams.

The left diagram contains three information. The black markers represent the measurement result regarding the projected fragment distance. The plot shows the distribution of the distances between deuterium and carbon monoxide in the detector plane. The second aspect considered by the left diagram are the distance distributions obtained by the simulation discussed in section 4.3.1. They are displayed as the dashed curves situated below the measurement result. Each curve results from an independently performed simulation. The third information contained in the left plot and the curve displayed in the plot on the right side provide additional details about these simulation results. Their sum is represented by the green curve which is the result of the fit routine. This routine weighs the simulated distance distributions and by this adapts their sum to the black marker plot.

The second diagram composes information about the input parameters of the simulation and the final result of the analysis. It shows the population density as a function of the kinetic energy release. Each of the horizontal lines corresponds to one of the simulated distance distributions in the left plot. They cover defined energy intervals. Based on these intervals the simulations have been performed. The vertical positions of the horizontal lines display concrete data concerning the fit result. They state the weight assigned to the single energy intervals. The more important the contribution of a simulated distribution

to the green curve is, the higher the corresponding horizontal line is situated and the higher the relative population of the states lying in this energy interval can be expected. In addition the right plot shows two vertical lines. They represent the energy position of the two electronically excited states of CO. If the kinetic energy release exceeds 0.38 eV, it can be excluded that the $a'\ ^3\Sigma^+$ state is populated because there is not sufficient excess energy available to reach such a high degree of inner excitation. In accordance the argumentation for the second line regarding the $a\ ^3\Pi_r$ state is the same.
Qualitatively it can be stated that there is an increased probability for the population of excited states. A quantitative analysis is complicated mainly due to two aspects. As section 4.1 has shown resorting to the results of the preliminary relaxation study the deuterated formyl cations are vibrationally excited with an average quantum number for the bending mode of $\nu_2 = 3$. This corresponds to an excitation of approximately 0.3 eV. Since the assignment of the excited states is based on the energy balance of the process the uncertainty about the initially available energy does not allow for an unambiguous identification of the states following the outlined argumentation. Moreover there is a multitude of vibrational states situated over the entire energy range [12]. These states certainly do not complicate to distinguish between the low vibrational excitation of the first electronically excited state $a\ ^3\Pi_r$ and an unlikely high vibrational excitation of the ground state $X\ ^1\Sigma^+$. Since the energy difference between both excited states is bridged by only four vibrational quanta misassignments may occur because the considerations do not distinguish between electronical and vibrational excitation.
Therefore the results remain restricted to the qualitative level clearly showing that the dissociative recombination of deuterated formyl cations into a deuteron and carbon monoxide preferentially leads to a relatively high inner excitation of the molecular recombination product.

5.1.2 Inner excitation of molecular fragments for elevated energies

The presentation of the data chosen in the previous section 5.1.1 can be adopted for elevated energies. In order to display the evolution of the projected distance distributions versus the energy a three-dimensional plot is used indicating the counts with the help of a color code. A slice at any fixed x-axis position in y-axis direction yields the distance distribution comparable to the measurement result shown in section 5.1.1 for the respective detuning energy. Due to insufficient statistics for the endoergic three-body channel and the (DO+C)-channel, which does not originate from the dissociative recombination

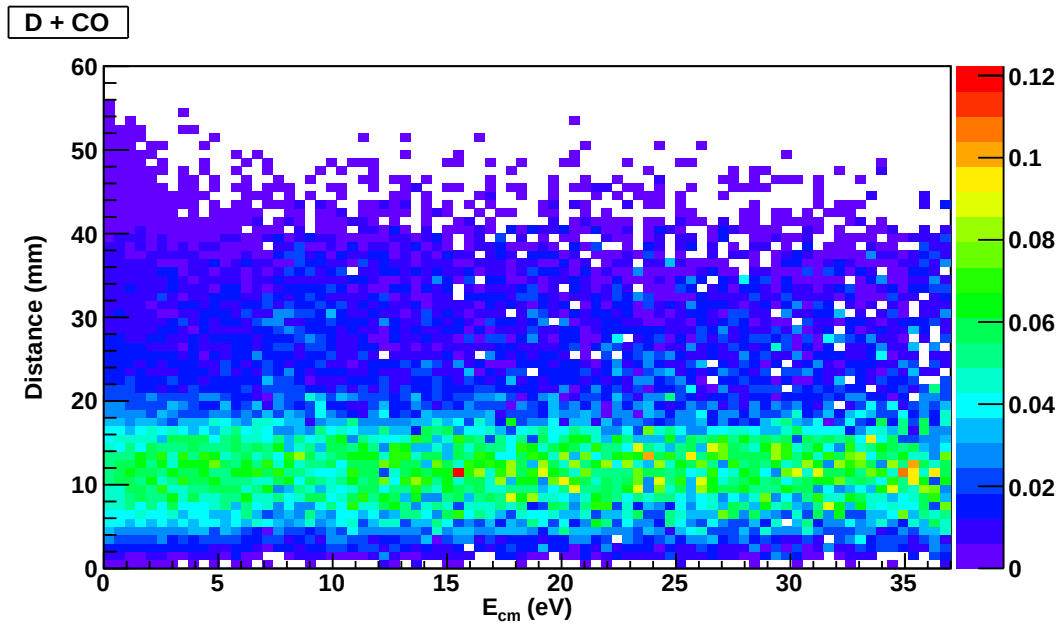

Figure 5.2: *Evolution of the distance distribution for the (D+CO)-channel investigating increasing detuning energies. Background distribution dominates over the entire energy range. The expected increase of the most probable projected fragment distance is not recognizable.*

of DCO^+ only the plots for the exoergic (D+CO)-channel and the fragmentation into DC and O are relevant.

The first plot is presented in figure 5.2 and shows the evolution of the projected fragment-distance distribution for the (D+CO)-channel.

As expected according to the considerations in section 4.3.2 the distribution is the same as for zero detuning energy since the channel is dominated by background events for elevated energies. There is no change detected in the evolution of the plot. A subtraction of the background events is not feasible because the distribution of the projected fragment-distance distribution has to be known for the background run. Because of insufficient statistics this distribution is indeterminable in the present study.

However the (DC+O)-channel enables to investigate the influence of increasing collision energies on the projected fragment distance distribution. For small energy values the background contribution is of manageable size and the statistics are sufficient for interpretation. Figure 5.3 displays the measurement data showing a clear drift of the most probable distance between the two particles in the detector plane for increasing detuning energy.

In the energy range up to 5 eV the statistics are reliable. While it is still possible to get an impression of the further evolution in the energy interval between 5 eV and 10 eV, the

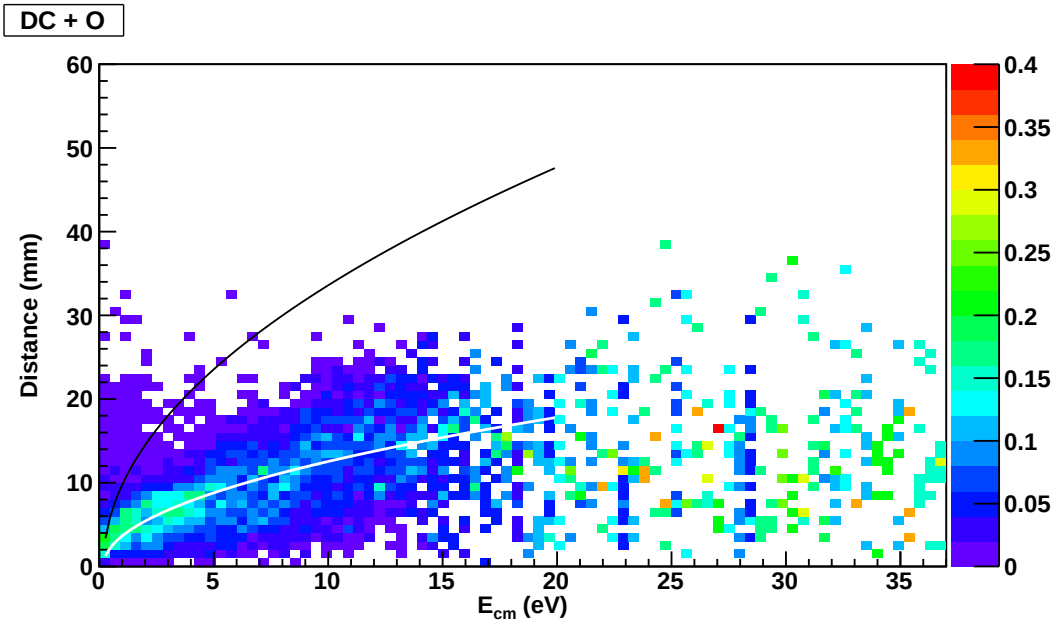

Figure 5.3: *Evolution of the distance distribution for the (DC+O)-channel investigating increasing detuning energies. The two graphs reflect the functional dependence between the detuning energy and the most probable fragment distance in the detector plane. The black curve evolution does not include an inner excitation of the molecular recombination product. The possibility of an inner excitation is taken into account by the white curve.*

recorded data do not allow for an interpretation for larger detuning energies.
In section 4.3.3 a formula has been derived for the largest possible distance between the center-of-mass of a two-body event and the lighter particle in this channel under strictly defined conditions. It has been found that this distance is proportional to the squareroot of the energy released in the dissociation process E_{KER}. Assuming that any further energy transferred to the system by the electron collision is additionally transformed into kinetic energy of the recombination products this formula can be written as

$$d = p \cdot \sqrt{E_{KER} + E_{cm}}$$

defining p as the proportionality constant, which comprises the following quantities.

$$p = D \frac{1}{\sqrt{E_{kin}}} \sqrt{\frac{m_1 + m_2}{m_1 \left(1 + \frac{m_1}{m_2}\right)}}$$

E_{kin} defines the beam energy and is considered as a constant. The two masses m_1 and m_2 are given by the fragmentation channel in focus. Thus the proportionality constant p only depends on the distance D between the point in the overlap region at which the electron

is captured and the detector. For the estimation of the upper limit for d this distance has been set to the maximum value. In the simulation discussed in section 4.3.1 D is chosen to give the average distance which corresponds to the center position assuming a uniform distribution of the breakup position along the overlap region.
For the black curve displayed in figure 5.3 this average distance $D = 9.41$ m has been chosen. If the detuning energy completely was transformed into kinetic energy, the evolution of the most probable distance between the particles, represented by the green and light blue squares, would follow this curve. Apparently this is not the case. In order to take into account the possibility of an inner excitation of the DC-fragment the parameter D is set to a smaller value, which is not compulsorily bound to an interpretation as significant distance. The curve corresponding to the latter choice of the parameter is colored white. It visualizes that the derived dependence between the distance evolution and the detuning energy holds. Since there are no clear deviations of the plot from this curve no electronically excited states of DC become energetically accessible in the energy range considered.
Figure 5.4 displays the evolution of the distance distribution focusing on the detuning-energy range between 0 and 5 eV. A variation of the parameter D leads to the thinner white curves above and below the curve, which is plotted in figure 5.3. These two additional curves also follow the evolution of the most probable distance in the regarded energy interval. There is no clearly defined value for the parameter D. No consistence is found for the energy range between 0 and 1 eV. The fragmentation channel (DC+O) is endoergic. Below 0.17 eV detuning energy the recorded events consequently originate from restgas collisions. The distribution of the distances between the fragments resulting from these collisions cannot be duplicated with the help of the derived function.

5.2 Branching ratios

A determination of the branching ratios into the different fragmentation channels is based on counting the total number of events and the number of events detected for the single channels. In accordance to the previous section the analysis of the branching ratios is presented separately for zero relative electron-ion collision energy in section 5.2.1 and for elevated detuning energy in section 5.2.2.
The results are compared to the most recent experimental results obtained applying the grid technique. This technique utilizes a grid with a known transmission which is located in front of a surface barrier detector. Measurements are performed with and without the grid. A comparison between the two measurements enables to reconstruct the probability

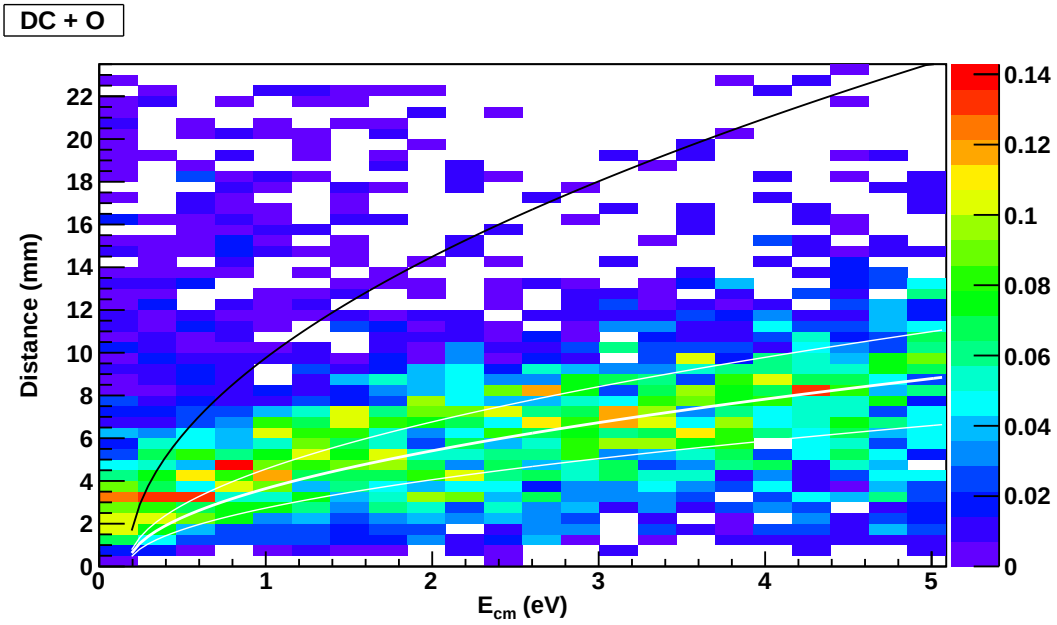

Figure 5.4: *Evolution of the distance distribution for the (DC+O)-channel focused on the detuning-energy range between 0 and 5 eV. The thinner white curves result from a variation of the parameter D.*

for the occurrence of the different dissociation pathways. A detailed introduction to the grid technique is given in [21].

For elevated detuning energy there are no experimental data for the branching-ratio evolution. In this case the analysis focuses on the comparison to the theoretically obtained results. The consistence of both approaches is checked showing clear indications for a correspondence regarding characteristic energy values at which the branching into certain channels gain importance and coincidently the calculated electronic resonant states become energetically accessible.

5.2.1 Branching ratios at zero relative electron-ion collision energy

At zero relative electron-ion collision energy the branching ratios are dominated by the fragmentation into the exoergic product channel (D+CO). In table 5.1 the results of the present study are listed.

They have been corrected for the different detection efficiencies using the correction matrix as discussed in section 4.3.1. Section 2.2.2 stated that the (DC+O)-channel is only accessible for deuterated formyl cations. Analogously the dissociation into (DO+C) can

Channel	DCO^+
D + CO	95.6 ± 1.5
DC + O	1.6 ± 1.0
DO + C	2.5 ± 0.4
D + C + O	0.3 ± 0.1

Table 5.1: *Branching ratios at zero relative electron-ion collision energy. The values have been corrected for the different detector efficiencies using the correction matrix.*

Channel	$D^{13}CO^+$ [22]	HCO^+ [23]	$H^{13}CO^+$ [24]
D + CO	88 ± 4	92 ± 3	87 ± 2
DC + O	6 ± 2	1 ± 1	4 ± 2
DO + C	6 ± 2	7 ± 2	9 ± 2

Table 5.2: *Branching ratios The assignment of the single fragmentation channels is kept in the original version for the purpose of a uniform presentation. In the various cases the fragments have different components, for example the D has to be replaced by an H.*

completely be assigned to the breakup of a deuterated isoformyl cation. Both isomers contribute in an unknown relation to the two remaining channels. The information about the branching ratios at zero detuning energy is completed by specifying the isomer abundance ratio of $\frac{[DCO^+]}{[DOC^+]} \approx 9$ as determined in the preliminary experiment presented in section 4.1. Merged-beam experiments applying the grid technique determined the branching ratios composed in table 5.2.

The various initial molecular ions, which differ from each other in their mass according to their composition of the single isotopes, are not considered to have a decisive influence on the branching into the fragmentation channels. As already outlined in the introduction of chapter 3 the electronic potential, which determines the molecule dynamics after the recombination, is the same for all four molecules. Only the reduced masses of the different systems are slightly modified, which is not considered as a reason for meaningful deviations in the branching ratios. Qualitatively the present experiment agrees with the three measurements in stating the order of the single channels. The (D+CO)-channel definitely is leading, the second exoergic channel being open only for the isomer is second followed by the (DC+O)-channel. However the deviations for these three channels, which allow a comparison, are remarkably high.

The grid technique does not enable an investigation of the branching ratio into the fourth

possible fragmentation channel. An assignment of an event to the three-body channel is not possible because the transmitted fragments from one of the two-body channels could also create the same signal impinging on the detector. Therefore the branching ratios of the three remaining channels are slightly overestimated.
The discrepancies between the three measurements probably can be explained by a different abundance ratio of the respective isomers in the single experiments. The branching ratios into the fragmentation channels (D+CO) and (DO+C) convey an idea of the abundance of the isomers. While in the experiment on $D^{13}CO^+$ the quotient of the branching ratios amounts to one, the experiment on HCO^+ leads to a clearly smaller value indicating that the relative amount of the isomers most likely is different in the various experiments. In order to enable a reliable comparison of the experiments the abundance ratio of the isomers should be added to the information about the branching ratios.

5.2.2 Energy dependence of the relative contributions

The energy dependent evolution of the relative contributions into the different fragmentation channels reveals the position of the resonant states. According to the considerations worked out in the previous chapters the branching into a single fragmentation channel rises when a corresponding resonant state becomes energetically accessible. The relative change in the relative contributions enables to identify these characteristic energy values and to assign them to resonant states within the resolution limitations set by the experimental technique and setup. Figure 5.5 shows the evolution of the relative contributions versus the detuning energy. As discussed in section 4.3.2 the y-axis label does not state 'branching ratio' but 'relative contribution' instead considering that the absolute values may be misleading. The error bars of the data points describing the (D+CO)-channel are increased by adding the systematic error determined in section 4.3.3.
The diagram shows the entire energy range covered during the measurements. Because of strongly decreased count rates for higher detuning energies it cannot be assured that the evolution of the graphs becomes increasingly affected by background events. A variation of the binning revealed that in the energy range from 25 eV to 40 eV the curve structure depends on the choice of the bin width. This is a consequence of insufficient statistics. A discussion of the features in the curve structures will be focused on the energy range for which the curve evolution is unambiguous and independent of any detail of its presentation.
As discussed in section 4.3.2 the determination of the relative contributions requires the subtraction of background events. The extent of this subtraction can be controlled by

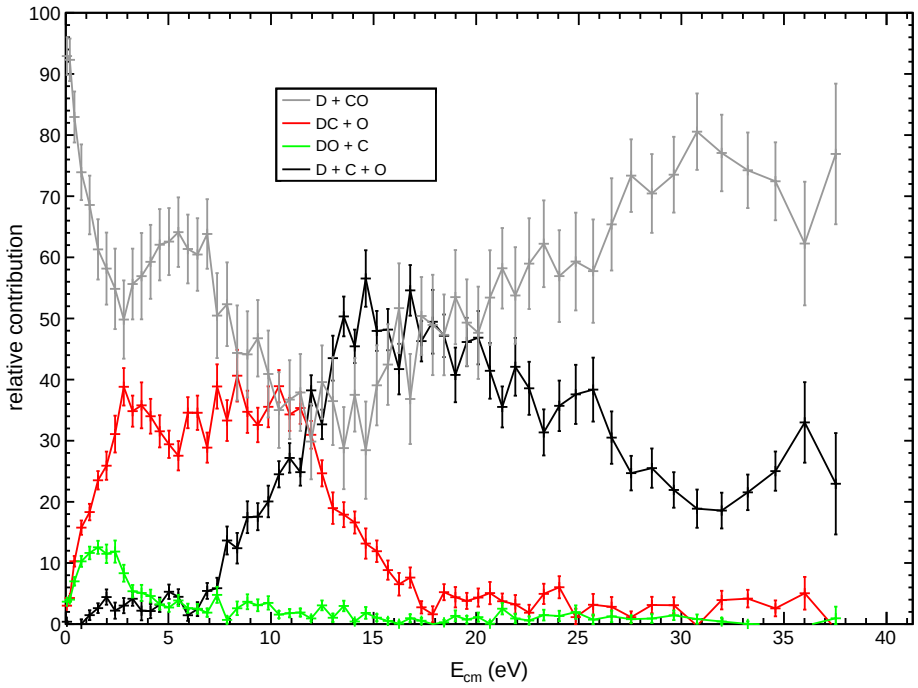

Figure 5.5: *Relative contribution versus detuning energy. The evolution of the curves for relative collision energy values greater than 25 eV depends on the choice of the binning.*

setting the parameter c. Figure 5.6 displays the corrected measurement results for the maximum value $c = 0.17$.

For the purpose of a clear presentation the parameter is set to $c = 0.1$. This does not alter the significance of the plot as discussed in 4.3.2. The corresponding plot is shown in figure 5.7. It is the basis for the following interpretations.

Starting at the values for zero detuning energy the branching into the (D+CO)-channel decreases as consequence of the increasing relative contributions of the other two-body channels. The (DO+C)-channel rises first, reaches its maximum and sinks to its initial level at relatively small energies again. The remaining two-body channel rises at higher energies and levels out at a sustained maximum. For further increasing energy values it also decreases returning to the initial value. The graph of the three-body channel shows a gradual rise starting at approximately 7 eV.

The features identified in the diagram can be interpreted on the basis of the findings presented in chapters 3 and 4 as follows.

1. The electronic resonant states of the deuterated isoformyl cation are lower in energy than the resonant states of the deuterated formyl cation. Consequently the

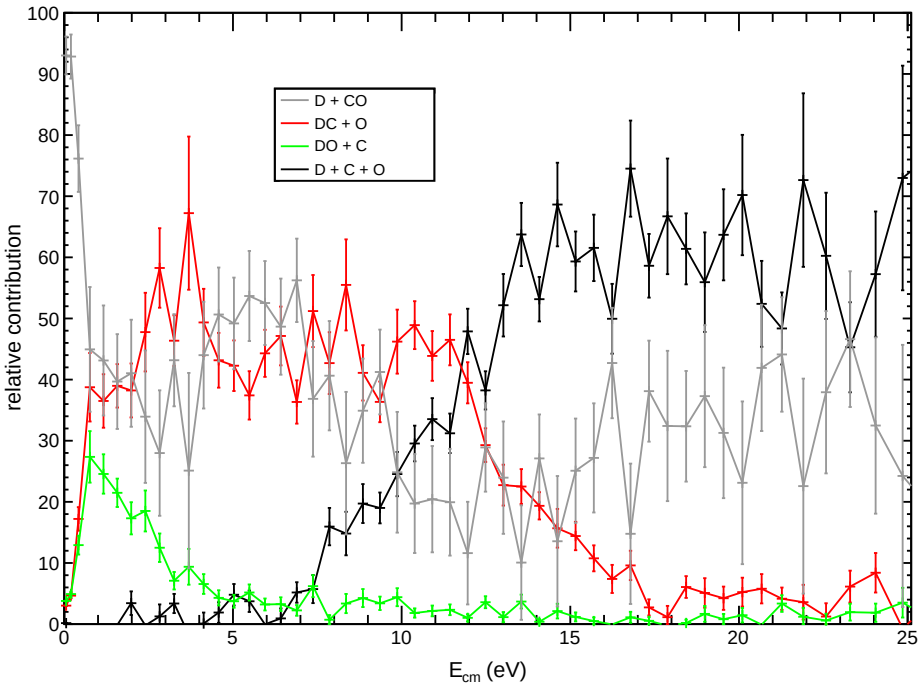

Figure 5.6: *Relative contribution versus detuning energy. The parameter c, which is the scaling parameter for the background subtraction introduced in 4.3.2, is set to its maximum value of 0.17.*

branching of the metastable isomer is enhanced for lower relative electron-ion collision energies, which is reflected by the start of the curve rise at relatively small energy values. The maintained linear geometry of the molecular ions assures that the green curve can be completely assigned to the fragmentation of DOC^+.

2. The relative contribution of the green curve representing the (DO+C)-channel can be traced back to the low abundance ratio of this isomer. Originally not intended to be abundant in the stored molecular ion beam, there is a small amount of DOC^+ because of the chosen production mechanism of the molecular ions discussed in section 4.2.1.

3. The red graph can be assigned to the breakup of DCO^+ correspondingly. The start and end position of the sustained maximum limit an energy interval, in which a dense range of electronic resonant states can be found.

4. The gradual rise of the three-body channel result from the fact that it is accessible starting from either DCO^+ or DOC^+. The contributions of the two production path-

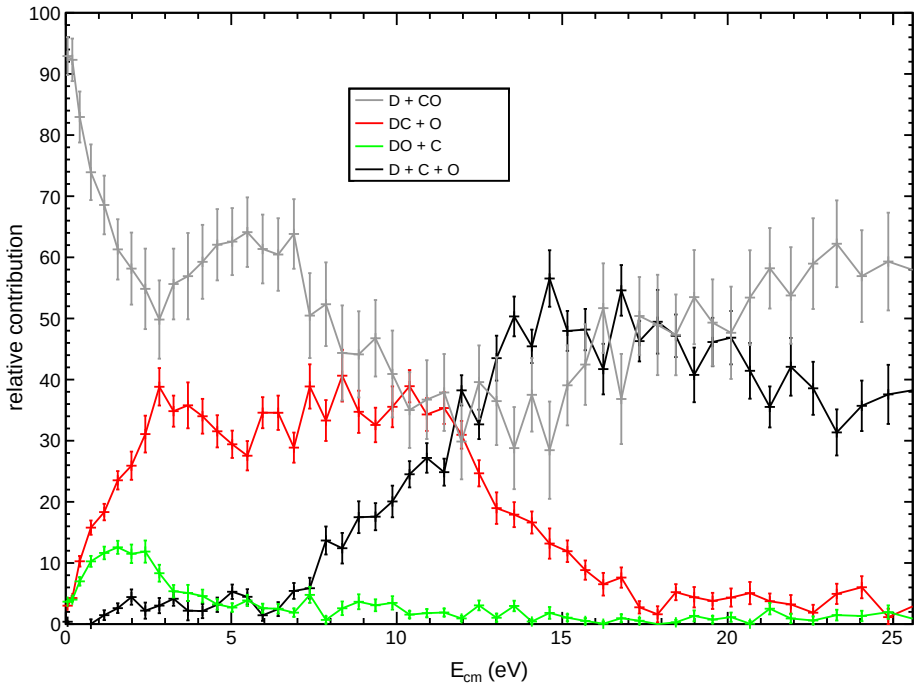

Figure 5.7: *Relative contribution versus detuning energy. The evolution of the curves is independent of the choice of the binning. The parameter c, which is the scaling parameter for the background subtraction introduced in 4.3.2, is set to 0.1 for the purpose of clearness.*

ways become relevant at different energy values corresponding to different situated resonant states.

There are no restrictions to the significance of the measurement results comprised in this diagram because of the uncertainties regarding the background estimations. The characteristic positions, at which the relative contributions of the single channels change, are not sensitive to any background correction. Thus the meaning and the position of the electronic resonant states can be checked on the basis of the experimentally obtained data.

5.3 Correspondence with resonant electronic potential surfaces

Based on the experimental results for the energy dependent evolution of the relative contributions the energy positions of the resonant states, which are derived by theoretical

calculations discussed in chapter 3, can be checked. In a first step the comparison between the simulated and the measured branching ratio evolution in the energy range from 0 to 8 eV conveys an idea whether the two approaches are consistent. As a reminder the simulation only takes into account the lowest resonant states calculated for HCO, while the experiment has been performed probing DCO. The effect of resonant states, which are situated higher in energy and not considered in the calculations, on the branching ratio evolution misses in the theoretical approach. Figure 5.8 displays the theoretical and experimental results. As discussed in section 4.3.2 the absolute positions of the single experimental curves are not certain. For the theoretical approach the same abundance ratio as determined for the experiment is assumed.

The trends of the evolution are consistent. The originally dominating channel containing D and CO as recombination products decreases as consequence of increasing contributions from the other two-body channels. It reaches its minimum and subsequently is subject to a slight recovery. The position of the minimum and the gradient of the subsequent rise do not match, but the qualitative evolution is reproduced correctly. This statement also holds for the evolution of the green and the red curve. In the experimental results there are no marked structures, which are recognizable in the theoretical results, but the rough structures can be found in both diagrams. In the case of the (DO+C)-channel the sharp peak at the beginning, representing the energy value at which the resonant states of DOC are accessible for the first time, while the resonant states for DCO are still energetically forbidden, is missing. The waved structure comprising three smaller maxima however can be detected in the experimental and the theoretical curves. Again the positions of these structures vary slightly. The comparison of the red curve evolutions fits to these findings. The rough structure is comparable, but there is no clear correspondence in detail. The rise of the three-body channel is steeper and starts at lower energy values in the case of the diagram containing the theoretical results.

The simulation of the branching ratio evolution resorts to the determination of the resonant states and employs the reduced mass of the formyl cations HCO. This reduced mass is increased in the case of deuterated formyl cations. Following the argumentation in chapter 3 the wavepacket, which is used to comprehend the dynamics of the dissociation process after a resonant state has been occupied, is more inert leading to a reduced mobility on the curves. Replacing the reduced mass in the simulation by the slightly modified value for deuterated formyl cations may correct for this difference in the comparison between the two approaches yielding a higher degree of correspondence.

To avoid this inconsistent aspect in the comparison the experimental result for the evolution of the relative contributions can be compared to the theoretical results in a prior

stadium which does not include the reduced mass as determining parameter. The energy positions of the resonant states should match the characteristic energy values for the rise of the corresponding curves. Figures 5.9 and 5.10 display the graphical comparison for the red and the green curve. The diagram on the left displays the experimental results. The other curves are taken from the representation of the theoretical data showing only the slices of the multidimensional potential energy surfaces for variable C-O coordinate. For each of these diagrams the potential energy surfaces as a function of variable D-C distance, or D-O distance respectively, are attractive and thus do not yield a breakup of these bonds.

In both cases the sustained maxima appear over energy intervals in which a dense range of electronic resonant states exist, which lead to the dissociation into the respective channels. The evolution of the graph describing the (DC+O)-channel continues on the same level going to energy values which are not considered in the theoretical calculations. This indicates that there might be resonant states situated immediately above the highest state calculated.

In figure 5.10 only the lowest resonant states of the respective symmetries have been resorted to in order to describe the maximum occurring in the green curve evolution. Since the experimentally obtained data do not show a second maximum, the resonant states higher in energy, which have been calculated for HOC, most likely do not indicate a dissociation of the O-C bond, which would contribute to the green curve.

Resonant states which are higher in energy and repulsive for both coordinates also explain the structure of the three-body channel.

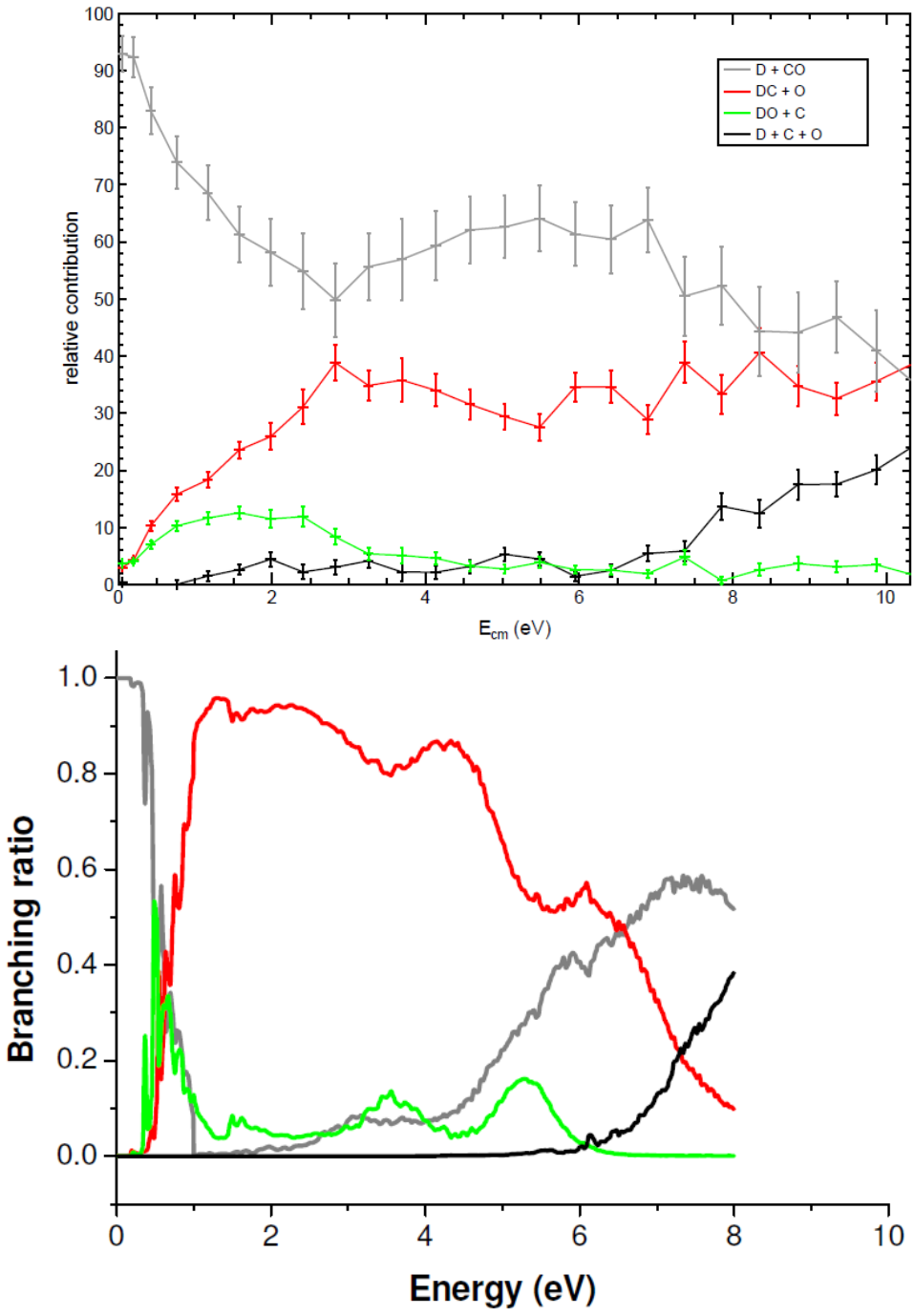

Figure 5.8: *Comparison between the simulated branching-ratio evolution and the experimentally obtained evolution of the relative contributions. Correspondence between the two approaches is indicated with regard to the rough curve structures and the detuning energy values, at which the single graphs begin to rise.*

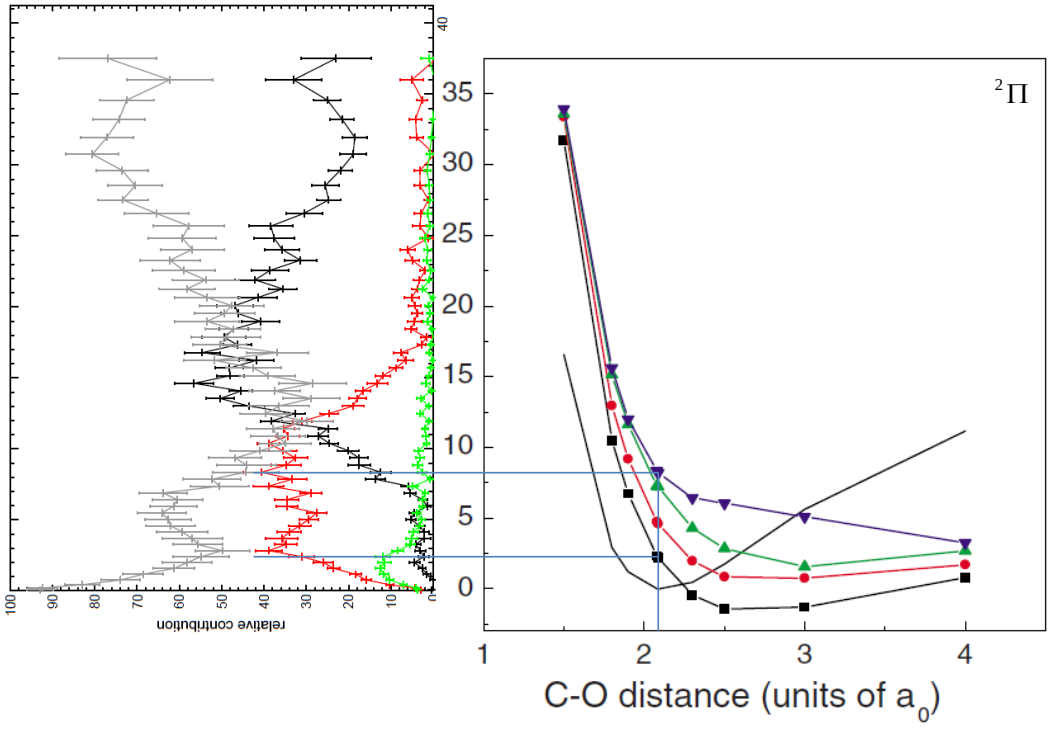

Figure 5.9: *Comparison between the energy positions of the electronic resonant states and the measured evolution of the relative contributions. The slices through the potential energy surfaces for* $^2\Pi$ *symmetry are displayed as a function of variable C-O coordinate. The states indicate dissociation into the channel containing DC and O, which is represented by the red curve. This curve shows a sustained maximum over an energy range, in which the lowest four resonant states lie. The further evolution of the experimentally obtained plot indicates that more resonant states probably are situated immediately above the calculated ones. The theoretical calculations have been carried out in [3].*

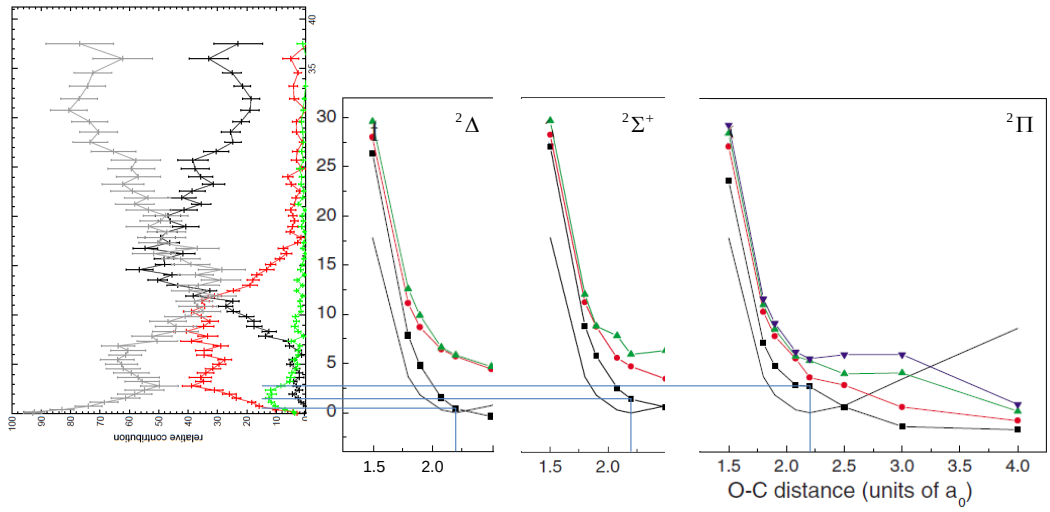

Figure 5.10: *Comparison between the energy positions of the electronic resonant states and the measured evolution of the relative contributions with regard to the fragmentation into DO and C. All three calculated symmetries of the DOC configuration are taken into account in order to point out the correspondence between the experimental and the theoretical approach. The maximum of the green curve in the left plot occurs over an energy range, which comprises the three energetically lowest resonant states.*

6. Summary and Outlook

The experimental investigations of the dissociative recombination applying the merged-beam technique provided by storage rings have been enhanced by the introduction of the energy-sensitive imaging detector EMU. It enables to detect multi-fragment events by coincidence imaging and simultaneously to identify the fragments by their masses. The EMU detector is predestined for an investigation of the branching ratios into the different fragmentation channels and their energy-dependent evolution. This evolution can be observed on an unprecedentedly wide energy range up to 25 eV. Despite the relatively low spatial resolution, which is defined by the width of the strips creating the special surface structure, the detector also enables investigations of the projected fragment-distance distributions. Utilizing these detector capabilities a molecular fragmentation study on the dissociative recombination of deuterated formyl cations has been performed.
An independent relaxation study on the molecular system, which has been performed in the run-up, provides essential information required for an interpretation yielding substantial results. In the present case the preparatory investigation applied the Coulomb explosion imaging technique resolving the questions of the inner excitation of the initial molecular ions and the abundance ratio of the isomer.
Besides a Monte-Carlo simulation of the uniformly distributed characteristics of the dissociation process, the propagation of the fragments and the varying detection efficiency for the different fragmentation channels is the key component for the analysis of the recorded data. It provides the information required to conclude from the measured to the real branching ratios and to extract the relative population of the excited states of the molecular recombination products from the observed projected fragment-distance distribution. The analysis of the present study was complicated because of events resulting from rest-gas collisions, which obscure the actual events originating from dissociative recombination. These background contributions predominantly affect the exoergic two-body channel (D+CO). They are negligible for investigations at zero relative electron-ion collision energy. Probing the dissociative recombination for elevated collision energies the measurement data has been corrected for the effects of the background events in an additional

analysis step. Moreover the background measurement should be performed until sufficient statistics are available to obtain the projected fragment-distance distribution of the events resulting from restgas collisions. The knowledge about this distribution enables to subtract the background contribution investigating the distribution of the fragment distances in the detector plane.

The focus of the analysis has been directed to the inner excitation of the molecular recombination products and the evolution of the relative contributions.

The inner excitation of the recombination product CO has been investigated for zero detuning energy. An increased probability for the population of electronically and vibrationally excited states has been found. A more detailed analysis which specifies the relative population of the single states could not be performed since the inner excitation of the deuterated formyl cations was uncertain and the multitude of vibrational levels of the carbon monoxide molecule did not allow for an unambiguous assignment of concrete transitions. The collision-energy dependent evolution of the projected fragment-distance distribution has been probed for the (DC+O)-channel. The measured evolution follows the expected function derived for the dependence of the most probable distance between the impact positions of DC and O on the detuning energy. Thus the population of an electronically excited state of DC, which becomes accessible for higher collision energies, has not been observed.

The comparison between the branching ratios at zero detuning energy determined within the present study to branching ratios obtained in experiments which applied the grid technique shows significant differences. Because of the insufficient compatibility of these former studies the discrepancy between the results on the experimental level have to be put into perspective. Due to the different characteristics of the dissociative recombination for the various isomers of the observed molecular system it is advisable to supplement the information about the branching ratios by specifying the abundance ratio of the isomer in order to enable a reliable comparison of the results. The energy-dependent evolution of the relative contributions indicates a correspondence to theoretical calculations of electronic resonant states which are considered a precondition for the occurrence of dissociative recombination. The branching ratio into a single fragmentation channel gains importance for detuning energy values at which electronic resonant states leading to the dissociation into this channel become energetically accessible.

The correspondence between the experimental and the theoretical approach of studying dissociative recombination is a convincing evidence that the achievements made so far have a guiding significance for further work on this essential molecular process. A more detailed check of the consistence requires the determination of the energy positions and

the structures of further resonant states by theoretical calculations. Besides a theoretical analysis of the process dynamics may help to avoid an argumentation based on the graphic results and to unambiguously disentangle which resonant state lead to the fragmentation into which channel. On the experimental level it is not possible to separate the deuterated formyl cations from their isomer. However a molecular fragmentation study is feasible utilizing a different method for the ion generation which leads to a various abundance ratio between the two isomers. The determination of this ratio would be subject to an experiment applying the Coulomb explosion imaging technique. If both complementary experiments, the relaxation study applying the latter technique and the concrete study of the dissociative recombination, are performed under identical systematic conditions, the contributions of the isomers to the fragmentation channels accessible for both of them can be probed resorting to the results of the present investigation.

The molecular fragmentation study on the dissociative recombination of deuterated formyl cations underlines the importance of storage-ring experiments applying the merged-beam technique for investigations on molecular dissociation processes. Advanced probes of the essential process characteristics are possible yielding unprecedented experimental results. These results provide the basis for astrophysical modeling which itself is the fundamental precondition for the interpretation of radioastronomical probes. An extension and a refinement of the latest findings on both the experimental and the theoretical level are necessary to support further progress on this sector of astrophysics.

References

[1] M. Larsson, A. E. Orel, *Dissociative Recombination of Molecular Ions*, Camebridge University Press, 2008.

[2] A. E. Orel, V. Ngassam, J. B. Roos, J. Royal and Å. Larson, *Resonances in dissociative recombination: trends and patterns*, Seventh International Conference on Dissociative Recombination, Journal of Physics: Conference Series 192 (2009), 2007, p. 012006.

[3] Å. Larson, A. E. Orel, *Electronic resonant states of HCO and HOC*, Phys. Rev. A **80** (2009), 062504.

[4] D. Buhl, L. E. Snyder, *Unidentified interstellar microwave line*, Nature **228** (1970), 267.

[5] W. Klemperer, *Carrier of the interstellar 89.190 GHz line*, Nature **227** (1970), 1230.

[6] M. Mladenović, S. Schmatz, *Theoretical study of the rovibrational energy spectrum and the numbers and densitites of bound vibrational states for the system HCO^+/HOC^+*, J. Chem. Phys. **109** (1998), 4456.

[7] R. Wester, et al., *Relaxation dynamics of deuterated formyl and isoformyl cations*, J. Chem. Phys. **116** (2002), 7000.

[8] H. Liszt, R. Lucas, J. H. Black, *Mm-wave HCO^+, HCN and CO absorption toward NGC1052*, Astron. Astrophys. **428** (2004), 117.

[9] D. R. Bates, *Dissociative Recombination*, Phys. Rev. **78** (1950), 492.

[10] J. C. Y. Chen, M. H. Mittleman, *The role of* R*ydberg states in dissociative recombination*, Fifth International Conference on the Physics of Electronic and Atomic Collisions (E. S. Solovyol I. P. Flaks, ed.), V ICPEAC, Leningrad, USSR, 1967, pp. 329–331.

[11] R. E. Rosati, Miroslaw P. Skrzypkowski, M. F. Golde, R. Johnsen, *Yield of excited CO molecules from dissociative recombination of HCO^+ and HOC^+ ions with electrons*, J. Chem. Phys. **126** (2007), 154302.

[12] P. H. Krupenie, S. Weissman, *Potential-Energy Curves for CO and CO^+*, J. Chem. Phys. **43** (1965), 1529.

[13] T. Amano, *The dissociative recombination rate coefficients of H_3^+, HN_2^+ and HCO^+*, J. Chem. Phys. **92** (1990), 6492.

[14] I. Korolov, R. Plasil, T. Kotrik, p. Dohnal, J. Glosik, *Recombination of HCO^+ and DCO^+ ions with electrons*, Int. J. Mass Spectrom. **280** (2009), 144.

[15] A. Le Padellec, C. Sheehan, D. Talbi, J. B. A. Mitchell, *A merged-beam study of the dissociative recombination of HCO^+*, J. Phys. B **30** (1997), 319.

[16] Å. Larson, Stefano Tonzani, Robin Santra and Chris H. Greene, *Dissociative recombination of* HCO^+, Sixth International Conference on Dissociative Recombination, Journal of Physics: Conference Series 4 (2005), 2005, pp. 148–154.

[17] D. Habs, et al., *First experiments with the Heidelberg test storage ring TSR*, Nucl. Instrum. Methods Phys. Res. B **43** (1989), 390–410.

[18] R. Wester, *Spatial structure of stored molecular ions by Coulomb explosion imaging*, Dissertation, Ruprecht-Karls-Universität Heidelberg, 1999.

[19] H. Buhr, et al., *A new energy-sensitive imaging detector - dissociative recombination of D_2H^+*, Phys. Rev. A **81** (2010), 062702.

[20] M. B. Mendes, *Molecular fragmentation by recombination with cold electrons studied with a mass sensitive imaging detector*, Dissertation, Ruprecht-Karls-Universität Heidelberg, 2010.

[21] S. Datz, et al., *Branching processes in the dissociative recombination of H_3^+*, Phys. Rev. Lett. **74** (1995), 896–899.

[22] W. Geppert, et al., *Extraordinary branching ratios in astrophysically important dissociative recombination reactions*, Faraday Disc. **127** (2004), 425–437.

[23] W. Geppert, R. Thomas, *Dissociative recombination branching ratios and their influence on interstellar clouds*, Sixth International Conference on Dissociative Recombination, Journal of Physics: Conference Series 4 (2005), 2005, p. 26.

[24] M. Hamberg, *Experimental studies on the dissociative recombination of* $H^{13}CO^+$ *with electrons at energies between 2-50000 meV*, Dissertation, Stockholm University, 2010.

Danksagung

Die Diplomarbeit ist im Rahmen einer einjährigen Beschäftigung am Max Planck Institut für Kernphysik entstanden. Für die umfassende Unterstützung, die ich bei der Durchführung und Auswertung des Experimentes und bei dem Verfassen der Diplomarbeit erfahren habe, möchte ich mich ausdrücklich bedanken.
Mein ganz besonderer Dank gilt Herrn Prof. Dr. Andreas Wolf für die Möglichkeit, die Diplomarbeit in seiner Arbeitsgruppe anzufertigen. Sein unentwegtes Engagement und die zahlreichen Denkanstöße haben eine umfassende und detaillierte Auseinandersetzung mit dem Thema in hohem Maße gefördert. Ein großer Dank auch für die Möglichkeit, an der DR-Konferenz teilzunehmen!
Die für die Interpretation erforderlichen Programme wurden von Dr. Henrik Buhr geschrieben. Er war darüber hinaus maßgeblich an der Entwicklung und Instandhaltung des Detektorsystems beteiligt. Danke für die kompetenten Hilfestellungen! Für die sehr hilfreichen kritischen Diskussionen, die die Auswertung des Experiments begleiteten, danke ich ebenso Prof. Dr. Dirk Schwalm, Dr. Oldrich Novotny und Dr. Mario Mendes.
Prof. Ann E. Orel und Prof. Åsa Larson danke ich für die Einsichten in die Auseinandersetzung mit dem Thema auf dem Gebiet der theoretischen Physik.
Die Durchführung eines Speicherring-Experimentes ist ohne die tatkräftige Unterstützung eines Teams aus Experten nicht denkbar. Es sei allen an den Strahlzeiten Beteiligten für die Überwachung des Speicherring- und Quellen-Betriebes und für die Übernahme von Tag- sowie insbesondere Nachtschichten gedankt.
Mein größter Dank gilt meinen Eltern, meinem Bruder und meiner Freundin Katrin. Vielen Dank, dass Ihr für mich da seid! Vielen Dank für den Rückhalt, den Ihr mir schenkt!

Erklärung

Ich versichere, dass ich diese Arbeit selbständig verfasst und keine anderen als die angegebenen Quellen und Hilfsmittel benutzt habe.

Heidelberg, den _____

_____

(Unterschrift)